



TAMPEREEN TEKNILLINEN YLIOPISTO  
TAMPERE UNIVERSITY OF TECHNOLOGY

**ALEKSI HIETANEN**

**UNTITLED**

Master's thesis

Examiner: John Doe

The examiner and topic of the thesis were approved on 11 September 2017



## **ABSTRACT**

**ALEKSI HIETANEN:** Untitled

Tampere University of Technology

Master of Science Thesis, 45 pages, 2 Appendix pages

October 2017

Master's Degree Programme in Science and Engineering

Major: Theoretical computer science

Examiner: John Doe

Keywords: Key, Word, List

**TODO**

## TIIVISTELMÄ

**ALEKSI HIETANEN:** Otsikoimaton

Tampereen teknillinen yliopisto

Diplomityö, 45 sivua, 2 liitesivua

Lokakuu 2017

Teknis-luonnontieteellinen diplomi-insinöörin tutkinto-ohjelma

Pääaine: Ohjelmistotiede

Tarkastaja:

Avainsanat:

**TODO**

## PREFACE

TODO

In Helsinki, Finland, on November 2, 2018

Aleksi Hietanen

## CONTENTS

1.	INTRODUCTION .....	1
2.	BACKGROUND AND RELATED WORK .....	4
2.1	Variational Autoencoders.....	4
2.1.1	Artificial Neural Networks .....	4
2.1.2	Autoencoders .....	7
2.1.3	Variational Inference.....	9
2.1.4	Autoencoding Variational Bayes .....	11
2.2	t-Distributed Stochastic Neighbor Embedding .....	13
2.2.1	SNE.....	13
2.2.2	t-SNE .....	15
2.2.3	Parametric t-SNE.....	17
3.	METHOD .....	19
3.1	Learning a Parametric Embedding Using VAE Sampling .....	19
3.2	Obtaining Reconstructions from Hidden Layers .....	20
3.3	Inference with the Generative Model.....	21
3.4	Robustness to Sparse and Noisy Data.....	21
3.5	Implementation .....	21
4.	EXPERIMENTS .....	23
4.1	Data Sets .....	23
4.1.1	MNIST .....	23
4.1.2	Fashion-MNIST .....	23
4.1.3	Mass Cytometry.....	23
4.1.4	Single-Cell RNA Sequencing .....	24
4.2	Evaluation Metrics .....	25
4.2.1	k-Nearest Neighbor Classifier.....	25
4.2.2	Trustworthiness.....	26
4.3	Network Structure and Parameters .....	26
4.4	Learning .....	27
4.5	Comparisons .....	28
4.5.1	Embedding Quality .....	29
4.5.2	Scalability .....	30
4.6	Robustness to Sparse Data .....	31
4.7	Robustness to Noisy Data .....	31
4.8	Obtaining Reconstructions from Hidden Layers .....	33
4.9	Inference with the Generative Model.....	34
4.10	Application to scRNA-seq Data.....	35
5.	CONCLUSIONS .....	38
	REFERENCES .....	39

APPENDIX A: SMALL BATCH SIZE, LOW PERPLEXITY EMBEDDING .....	46
APPENDIX B: UMAP EMBEDDING OF SCRNA-SEQ DATA .....	47

## LIST OF FIGURES

<b>Figure 2.1.</b>	<i>Feedforward neural network with input dimension 3, output dimension 2 and 2 hidden layers of dimension 4 each. ....</i>	6
<b>Figure 2.2.</b>	<i>Autoencoder .....</i>	8
<b>Figure 2.3.</b>	<i>Illustration of the mean-field approximation of a full rank Gaussian. Adapted from [7], Figure 1.....</i>	10
<b>Figure 2.4.</b>	<i>The VAE graphical model, in plate notation. Adapted from [38], Figure 1. ....</i>	11
<b>Figure 2.5.</b>	<i>Variational Autoencoder .....</i>	13
<b>Figure 4.1.</b>	<i>Voronoi diagram illustrating the decision boundaries of 10 different classes of a 1-NN classifier. Black dots represent the training data points, and the different colors correspond to the label of the data point for that region. Any point to be classified would receive the label corresponding to the location in the tessellation it lies on. The distance metric used in this example is the Euclidean distance.....</i>	25
<b>Figure 4.2.</b>	<i>Plots of 1-NN and trustworthiness scores obtained after a given number of iterations for different batch sizes. The means and 95% confidence intervals have been plotted from 20 repeated runs for each parameter setting. ....</i>	28
<b>Figure 4.3.</b>	<i>Embeddings of the MNIST data set trained with batch size 400.....</i>	29
<b>Figure 4.4.</b>	<i>Embeddings of the Fashion-MNIST data set trained with batch size 400. [Note: could include UMAP embedding of this data set here for comparison. It is remarkably similar and this would reinforce the claim that small batch size training is actually very effective.] .....</i>	29
<b>Figure 4.5.</b>	<i>Cytometry A data set embedded with the methods being compared in section 4.5. ....</i>	32
<b>Figure 4.6.</b>	<i>1-NN and trustworthiness scores obtained for PTSNE and VPTSNE trained on small subsets of the MNIST data set. Error bars indicate the 95% confidence intervals of the mean for each sparsity level, obtained from 20 repeated runs. ....</i>	33
<b>Figure 4.7.</b>	<i>1-NN and trustworthiness scores obtained for PTSNE and VPTSNE trained on MNIST data with different levels of masking noise applied. Error bars indicate the 95% confidence intervals of the mean for each corruption level, obtained from 20 repeated runs. ....</i>	33
<b>Figure 4.8.</b>	<i>Embedding produced by training on a 7 dimensional latent representation of the MNIST data set contrasted with the result of the original PTSNE implementation. VPTSNE trustworthiness: 0.927, 1-NN: 0.910. PTSNE trustworthiness: 0.926, 1-NN 0.887. ....</i>	34
<b>Figure 4.9.</b>	<i>Detecting outliers in cytometry data. [Rename patients to match text.]</i>	35
<b>Figure 4.10.</b>	<i>Visualization of analysis results on data from [70] using VPTSNE.....</i>	37



<b>Figure A.1.</b>	<i>Effect of the choice of perplexity w.r.t. batch size. MNIST VPTSNE embedding trained with batch size 200 and perplexity 10. Trustworthiness: 0.935, 1-NN: 0.812. ....</i>	46
<b>Figure B.1.</b>	<i>Visualization of analysis results on data from [70] using UMAP. ....</i>	47

LIST OF TABLES

*Table 4.1.*      *Comparison between different dimensionality reduction methods. ....* 31

## LIST OF SYMBOLS AND ABBREVIATIONS

GPU	graphics processing unit
GPGPU	general-purpose computing on graphics processing units
TPU	tensor processing unit
PCA	principal component analysis
AE	autoencoder
VAE	variational autoencoder
UMAP	uniform manifold approximation and projection
SNE	stochastic neighbor embedding
t-SNE	t-distributed stochastic neighbor embedding
k-NN	k-nearest neighbors
RNA	ribonucleic acid
scRNA-seq	single-cell RNA sequencing
$\mathcal{N}(\mu, \Sigma)$	Gaussian distribution with mean $\mu$ and covariance $\Sigma$
$p(x y)$	conditional probability of $x$ given $y$
$\sim$	is distributed as
$\frac{\partial}{\partial x}$	partial derivative w.r.t. $x$
$D_{\text{KL}}(p \parallel q)$	Kullback-Leibler divergence from $p$ to $q$
$\mathbb{E}_p[q]$	Expectation of $q$ under distribution $p$



# 1. INTRODUCTION

At present, ever larger sets of increasingly higher dimensional data are being produced, gathered and analyzed. As a consequence, several challenges arise when analyses are carried out on these vast amounts of high dimensional data. This recent surge of data prompts not only for the development of methods for data analysis capable of scaling to massive data sets but ones which are simultaneously capable of dealing with challenges inherent to high dimensional data.

In literature, problems arising from high dimensionality are collectively referred to as the *curse of dimensionality*, a term first coined by Richard Bellman in the context of dynamic programming [6]. Particularly in machine learning the following aspects of high dimensionality

- distances between pairs of points become less distinguished as dimensionality of the space increases [2], rendering methods based on distance metrics at a disadvantage.
- The volume of a space grows exponentially along with the number of dimensions. This leads to even large data sets appearing sparse in the feature space. Efficient sampling requires a lot of points
- need for more training data, k-means example [62, p. 263]
- algorithm complexity depends on the dimensionality of data being processed, large costs are accrued
- from a more practical perspective, high dimensional data by itself is hard to directly reason about and difficult to visualize in any meaningful sense, as simple statistics will often not be able to capture adequate information of the data distribution.

The given listing is not exhaustive, but rather serves as an illustration for the variety of issues that can be encountered when working with high dimensional data.

To tackle problems associated with high dimensional data a common approach is to seek for a lower dimensional representation of the data which retains its salient features. This process, known as dimensionality reduction, can be split into two different approaches, namely *feature selection* and *feature extraction*.

The so-called manifold hypothesis [52] often holds for real-world data sets. The manifold hypothesis posits that the high dimensional data in question lies near a much lower dimensional manifold. As an example, take ... . This in turn implies that if it is possible to learn this manifold, the original data could be described in far fewer dimensions with minimal loss of information. This, together with the classical Johnson-Lindenstrauss

lemma [31], which provides general bounds to the error associated with dimensionality reduction between points of two Euclidean spaces, give a strong indication that for many data sets substantial dimensionality reduction is not only feasible, but that most of the information within the data can be captured with fewer parameters.

Several different methods for dimensionality reduction have been developed over the years. Arguably the most well known and applied dimensionality reduction method in practice is Principal Component Analysis (PCA), developed independently by Karl Pearson [19] and Harold Hotelling [28] in the early 1900s. Although very efficient to compute and providing easily interpretable results, PCA however suffers from the fact that it only takes into account linear relationships in the data it is given, making it nonideal for ... . The fact that PCA only aims to find an orthogonal projection that maximizes the variance... local structure of the data is poorly preserved. On the other hand, methods that aim to preserve local structure of data typically suffer from poor scalability to large data sets and the curse of dimensionality in several ways, such as ... .

As a wealth of dimensionality reduction methods have been developed, attempting to cover all of them would be greatly out of the scope of this thesis, in which the focus is on improving an existing method for primarily data visualization purposes. For comprehensive reviews on other prominent methods the reader is referred to [47, 8].

In exploratory data analysis, visualization of the characteristics of data sets plays a key role. Being able to project high dimensional data into meaningful low dimensional representations enables researchers and data analysts to generate hypotheses.

In this work, a method for improving the applicability of parametric t-SNE is proposed. In the proposed method a generative model in the form of a Variational Autoencoder is first trained and subsequently used to produce training data for the parametric t-SNE embedding. The benefits of this procedure are severalfold: . Further, each of these benefits are experimentally demonstrated on a variety of data sets, both quantitatively and qualitatively.

The structure of this thesis is as follows. In Chapter 2 the relevant background and related work to the contribution of this thesis is covered to give context to an audience not previously familiar with variational autoencoders or the t-SNE method for dimensionality reduction. The chapter is organized into two main sections, one that builds up to the theory and recent advances in variational autoencoders from the introduction of neural networks, and the other section presents the development of t-SNE up to its parametrization with neural networks.

The method developed for this thesis is presented in Chapter 3. The proposed learning and inference algorithms are presented, together with discussion on extensions and further variations. In addition, relevant implementation details of the application built to produce the results for the experiments chapter are briefly covered.

In Chapter 4 the proposed method is tested experimentally for different properties presented in the previous chapter, as well as compared with existing methods. The experiments chapter includes descriptions for the various data sets being used and definitions for the metrics employed to quantitatively assess the quality of the produced low dimensional embeddings by our method and other methods under comparison.

The final chapter presents discussion and conclusions for the work carried out in this thesis. Additionally, directions for future work are suggested.

## 2. BACKGROUND AND RELATED WORK

- main motivator for this work is to provide a tool to enhance exploratory analysis in cancer research
- on molecular data
- find references where visualization is used to aid analysis
- discuss current state of the art
- challenges associated with currently used methods
- we outline in this chapter the relevant background information on the two methods that are used in the developed method, discussed in chapter 3

### 2.1 Variational Autoencoders

An essential component of the method presented in this work are Variational Autoencoders (VAEs). VAEs belong to a broad class of models termed deep generative models, which have in recent years played an important role in machine learning research. As their name suggests, generative models attempt to model the process by which a given set of data has been generated by learning the underlying distribution of the data. Deep generative models are distinguished by the property that they are parameterized by neural networks, enabling the use of deep learning methods.

[Note: short history of methods developed, RBM/DBN/DBM/GAN...]

[Note: Thorough review of deep generative models mentioned here, but which are out of scope for this work, can be found in [22, Chapter 20].]

Before moving on to specialized artificial neural network structures and learning objectives, a brief review of the relevant background literature is presented. First, a general introduction to artificial neural networks is given, after which autoencoder neural networks are discussed in more detail. The theory and purpose of variational Bayesian methods are discussed to finally arrive at the full definition of VAEs by bringing together the contents of the preceding sections.

#### 2.1.1 Artificial Neural Networks

Artificial neural networks, or as commonly referred to simply as neural networks, are a computational framework inspired by the biology of animal brains, more specifically the interconnected structure of individual nerve cells. Not unlike their biological counterparts,



neural networks are composed of individual neurons capable of processing and passing along signals from one another to perform complex computation tasks as a whole.

Neural networks are at the core of many recent advances in machine learning. Particularly, deep neural network architectures now hold many state-of-the-art results in fields including computer vision, natural language processing, and speech recognition [40]. More broadly, neural networks have been applied to all different categories of machine learning tasks, i.e. supervised, semi-supervised, unsupervised and reinforcement learning, with great success.

Advances in supervised learning for computer vision have arguably played an important role in the development of modern machine learning. [16].

Unsupervised and semi-supervised learning, representation learning. Deep belief networks, or rather unsupervised pretraining by stacking RBMs is one of the most important results in reviving interest in deep learning, as it was one of the first generally applicable results to enable learning of deep networks.

Reinforcement learning, atari [51], go [63] and shortly after, go *tabula rasa* [64].

The development of ever faster hardware for accelerating the computations needed for deep learning has played a pivotal role in the resurgence of research interest in neural networks. Originally built to accelerate the linear algebra operations required to produce 3D computer graphics, graphics programming units (GPUs) offer immense parallel computing capabilities compared to traditional central processing units (CPUs). With the advent of programming languages and APIs targeting GPUs, general-purpose computing on this specialized hardware has been made possible and has subsequently been taken advantage of in research and development of applications making use of neural networks. Recently, hardware specialized solely for use with deep learning has been developed [32] and microarchitectures of modern GPUs have begun to incorporate specialized computing units for deep learning [49], indicating a strong and growing interest towards deep learning in both academia and industry alike.

## Structure of Neural Networks

Neural networks can be thought of as being large function compositions. Each neuron that is part of the network acts as a single function, taking as input the weighted output of other neurons connected to it and outputting the value of the neuron's *activation function*. Neural networks can be classified into two main categories: feedforward and recurrent neural networks. Thinking of neurons and their connections in terms of graphs, where neurons represent vertices and edges represent the flow of data from one neuron to another, these two categories correspond to acyclic directed graphs and directed graphs that may contain cycles. In this work we will limit our focus to feedforward neural networks as the methods discussed do not make use of recurrent neural network structures.

As an example, Figure 2.1 depicts a feedforward neural network<sup>1</sup> taking input vectors  $\mathbf{x}$  of length 3 and outputting vectors  $\mathbf{y}$  of length 2. The network can be seen to be split into three functionally distinct parts: an input layer, hidden layers, and an output layer. The input layer is directly fed the values to be run through the network. The hidden layers are formed by neurons connecting the input to the output layer. The output layer represents the result of the computation performed by the network. What this depicted neural network computes can be expressed with the equation

$$\mathbf{y} = f_3(\mathbf{W}_3 f_2(\mathbf{W}_2 f_1(\mathbf{W}_1 \mathbf{x} + \mathbf{b}_1) + \mathbf{b}_2) + \mathbf{b}_3),$$

where  $f_i$  are the activation functions,  $\mathbf{W}_i$  the matrices of weights, and  $\mathbf{b}_i$  the biases of the  $i$ th layer. The purpose of an activation function is to alter incoming signals to induce nonlinearity into the network as well as impose constraints on the values that flow through specific neurons, enabling the learning of more complex functions with desired properties. Bias neurons enable the shifting of activation function outputs. Weights of the network control the signal strengths from one neuron to the other.

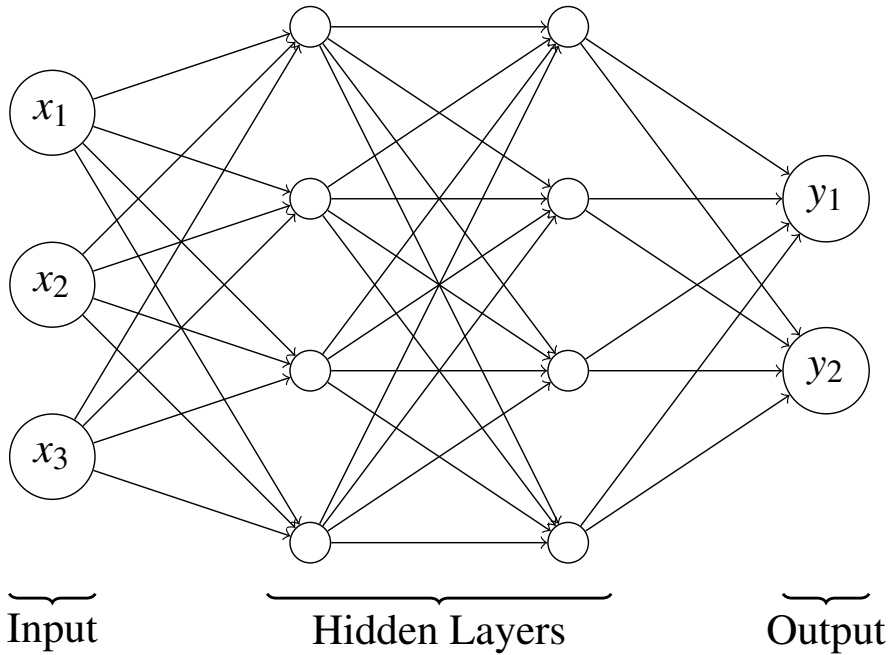


**Figure 2.1.** Feedforward neural network with input dimension 3, output dimension 2 and 2 hidden layers of dimension 4 each.

## Learning in Neural Networks

A simplistic view of neural networks would be to consider them merely as powerful function approximators. The theoretical underpinning for this view is the universal approximation theorem [27], which states that under mild conditions on the activation function,

<sup>1</sup>Note that bias neurons are omitted from the figure for simplicity.

neural networks with a single hidden layer can arbitrarily well approximate any continuous function.<sup>2,3</sup> However, the universal approximation theorem does not state anything about the challenges associated with the learnability of the parameters for these approximations, which is where many of the practical challenges associated with neural networks lie.

Learning in neural networks boils down to the efficient finding of correct weights for the network to produce desired outputs for given inputs. How well a given network performs is evaluated by computing the value of its *objective function*, given the knowledge of the input and output values. Finding weights for a given network thus becomes a problem of optimizing the value of its objective function.

Neural networks can be trained for various different computational tasks by simply choosing the correct objective function. Perhaps the most common use case for neural networks is to use them for classification.

Early on in the development of neural networks the simple yet powerful backpropagation algorithm was developed independently by multiple researchers and later popularized by Rumelhart et al. [60] to enable the efficient training of neural networks. In essence, backpropagation is an algorithm to perform gradient descent to optimize neural network weights by exploiting the compositional structure of neural networks and the chain rule of derivatives.

The backpropagation algorithm proceeds as follows: first, input values are run through the entire network to compute the value of the objective function.

[Note: Backprop algorithm in more detail, SGD, gradient descent optimization methods (mention second order methods?)]

Several difficulties still arise in the optimization of neural networks. [Note: explain some of the recent research regarding convergence, vanishing gradients, momentum based methods, regularization, training deeper networks ... [30, 67, 21, 23], and how there still isn't consensus on why some established methods seem to work ([61]) (learning rate/batch size choice for optimization [34, 65]) (potentially worse generalization of adaptive gradient methods, such as AdaGrad, RMSProp, Adam [77])]

### 2.1.2 Autoencoders

First discussed in [59] as "the encoding problem".

Efficient training via stacking RBMs described in [26], as well as its capabilities for dimensionality reduction.

<sup>2</sup>The universal approximation theorem requires that the activation function is nonconstant, bounded and continuous, which highlights the importance of nonlinear activation functions.

<sup>3</sup>To be precise, this approximation applies to continuous functions defined on compact subsets of  $\mathbb{R}^n$ .

The learning objective of autoencoders is to reconstruct the original input data as faithfully as possible. [Note: Common objective function is to minimize the mean squared error:]

$$\mathcal{L}_{MSE} = \frac{1}{N} \sum_{i=1}^N \left\| \mathbf{x}^{(i)} - \hat{\mathbf{x}}^{(i)} \right\|^2. \quad (2.1)$$

[Note: Structure consists of two parts, the encoder and decoder. An example autoencoder network has been visualized in Figure 2.2.]

[Note: Trivial case, where the network has too much capacity the AE can simply learn the identity function. Not useful for learning hidden representations, i.e. meaningful latent codes.]

[Note: Case where the latent code's dimensionality is smaller than the original data's dimensionality. This *bottleneck* potentially discards data, leading to a *lossy compressed* representation.]

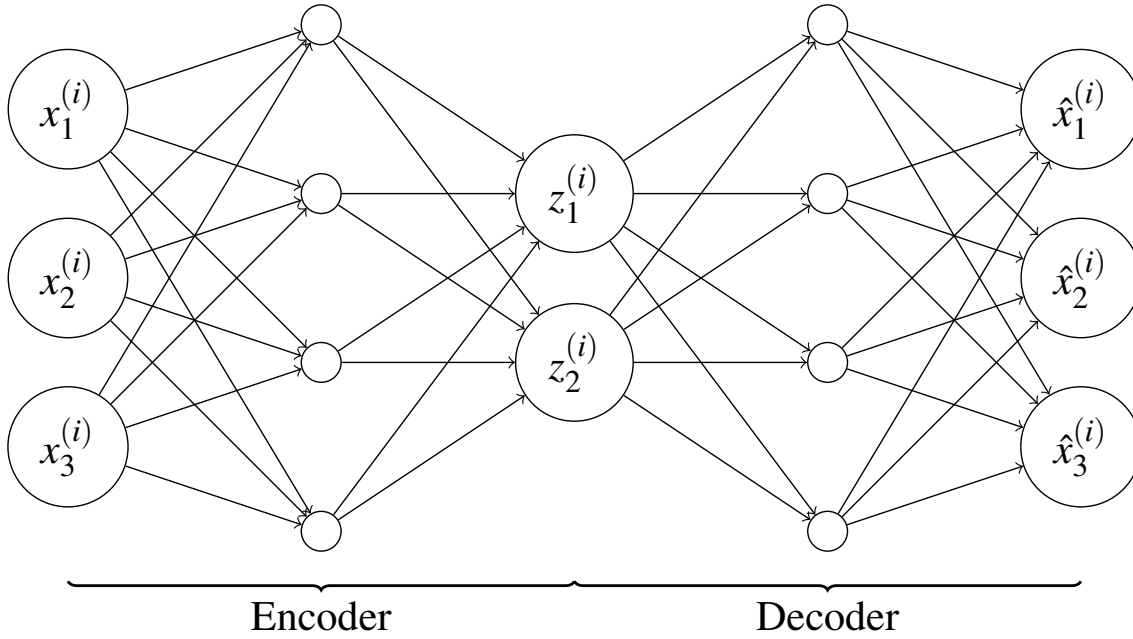


**Figure 2.2.** Autoencoder

A connection between PCA and autoencoders which are constrained to only have linear activation functions and are optimized with the MSE objective (see Equation 2.1) has been shown in [4]. [Note: The subspace spanned by the first  $d'$  principal eigenvectors of the (combined) weight matrix is equivalent to the first  $d'$  principal components of the training data. The latent code of such an autoencoder is an orthogonal projection onto this subspace. Additionally, the optimization problem is convex.]

[Note: Elaborate potential downsides of this approach (how to interpret the learned representation when nonlinearity is introduced? how does it generalize?). This is set up for why stochastic autoencoders are desirable.]

### 2.1.3 Variational Inference

In modern statistics and machine learning a need to approximate highly complex probability distributions is a problem that often arises as Highly complex probability densities often arise in modern statistics and machine learning. A core challenge that arises in modern statistics and machine learning is that of approximating

A domain where such complex distributions are often encountered is Bayesian inference, where the posterior

The Bayes theorem states that the posterior distribution is given by

$$p(\mathbf{z}|\mathbf{x}) = \frac{p(\mathbf{z}, \mathbf{x})}{p(\mathbf{x})} = \frac{p(\mathbf{z}, \mathbf{x})}{\int p(\mathbf{z}, \mathbf{x}) d\mathbf{z}}.$$

Even for only moderately complex models exact computation of the posterior is often intractable due to the required marginalization over all possible latent values  $\mathbf{z}$ . To illustrate this problem we will consider the Bayesian mixture of Gaussians model as in [7]. The model under consideration is univariate and consists of  $K$  unit variance Gaussian mixture components. The full hierarchical model is given by the following

$$\begin{aligned}\mu_k &\sim \mathcal{N}(0, \sigma^2), \\ c_i &\sim \text{Categorical}\left(\frac{1}{K}, \dots, \frac{1}{K}\right), \\ x_i | c_i, \mu &\sim \mathcal{N}(c_i^\top \mu, 1).\end{aligned}$$

From these definitions, the joint distribution factorizes as

$$p(\mu, \mathbf{c}, \mathbf{x}) = p(\mu) \prod_{i=1}^n p(c_i) p(x_i | c_i \mu).$$

Now, when marginalizing out  $\mu$  and  $\mathbf{c}$ , we arrive at the following integral

$$p(\mathbf{x}) = \int p(\mu) \prod_{i=1}^n \sum_{c_i} p(c_i) p(x_i | c_i \mu) d\mu.$$

As the time complexity of evaluating this integral is  $\mathcal{O}(K^n)$ , it is evident that direct computation quickly becomes infeasible even for relatively small  $K$  and  $n$ .

The dominant paradigm for obtaining these approximates has been through various methods of sampling.

Variational inference takes a different approach to approximating the posterior. Instead of sampling, in variational inference the approximation problem is turned into an optimization problem. By considering a family of distributions  $\mathcal{Q}$

$$q^*(\mathbf{z}) = \arg \min_{q(\mathbf{z}) \in \mathcal{Q}} D_{\text{KL}}(q(\mathbf{z}) \parallel p(\mathbf{z}|\mathbf{x}))$$

[Note: It is possible to combine automatic differentiation with variational inference to further ease statistical model building and computational efficiency [39]. (Brief discussion on probabilistic programming)]

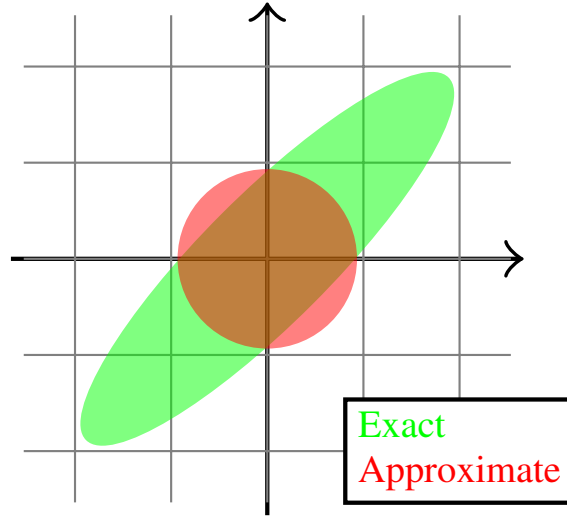


**Figure 2.3.** Illustration of the mean-field approximation of a full rank Gaussian. Adapted from [7], Figure 1.

## Kullback-Leibler Divergence

The Kullback-Leibler divergence, or KL-divergence for short, is a measure of dissimilarity between two probability distributions.

For continuous probability distributions  $p$  and  $q$  the Kullback-Leibler divergence is defined as

$$D_{\text{KL}}(p \parallel q) = \int p(\mathbf{x}) \log \frac{p(\mathbf{x})}{q(\mathbf{x})} d\mathbf{x},$$

and likewise for discrete probability distributions as

$$D_{\text{KL}}(p \parallel q) = \sum_i p(i) \log \frac{p(i)}{q(i)}.$$

The following properties hold for KL-divergence:

1.  $D_{\text{KL}}(p \parallel q) \geq 0$  (non-negativity)
2.  $D_{\text{KL}}(p \parallel q) = 0 \iff p = q$  (identity of indiscernibles).

One must note however that KL-divergence is asymmetric, i.e.  $D_{\text{KL}}(p \parallel q) \neq D_{\text{KL}}(q \parallel p)$ , and does not obey the triangle inequality, thus cannot readily be used as a metric. Especially asymmetry is important to take into account when interpreting the use of KL-divergence.

## The Evidence Lower Bound

### 2.1.4 Autoencoding Variational Bayes

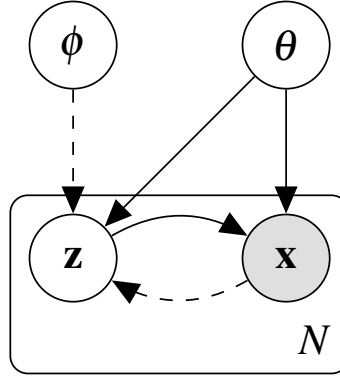


**Figure 2.4.** The VAE graphical model, in plate notation. Adapted from [38], Figure 1.

## Derivation of the VAE Objective Function

The objective of VAEs is to model the data as well as possible, i.e. maximize the marginal likelihood  $p_\theta(\mathbf{x}^{(i)})$  for each data point  $i$ . By an application of Jensen's inequality we can derive the following lower bound for the marginal likelihood under our latent variable model:

$$\begin{aligned}
 \log p_\theta(\mathbf{x}^{(i)}) &= \log \int p_\theta(\mathbf{x}^{(i)} | \mathbf{z}) p(\mathbf{z}) d\mathbf{z} \\
 &= \log \int \frac{q_\phi(\mathbf{z} | \mathbf{x}^{(i)})}{q_\phi(\mathbf{z} | \mathbf{x}^{(i)})} p_\theta(\mathbf{x}^{(i)} | \mathbf{z}) p(\mathbf{z}) d\mathbf{z} \\
 &= \log \mathbb{E}_{q_\phi(\mathbf{z} | \mathbf{x}^{(i)})} \left[ \frac{p_\theta(\mathbf{x}^{(i)} | \mathbf{z}) p(\mathbf{z})}{q_\phi(\mathbf{z} | \mathbf{x}^{(i)})} \right] \\
 &\geq \mathbb{E}_{q_\phi(\mathbf{z} | \mathbf{x}^{(i)})} \left[ \log \frac{p(\mathbf{z})}{q_\phi(\mathbf{z} | \mathbf{x}^{(i)})} \right] + \mathbb{E}_{q_\phi(\mathbf{z} | \mathbf{x}^{(i)})} \left[ \log p_\theta(\mathbf{x}^{(i)} | \mathbf{z}) \right] \\
 &= -D_{\text{KL}}(q_\phi(\mathbf{z} | \mathbf{x}^{(i)}) \parallel p(\mathbf{z})) + \mathbb{E}_{q_\phi(\mathbf{z} | \mathbf{x}^{(i)})} \left[ \log p_\theta(\mathbf{x}^{(i)} | \mathbf{z}) \right].
 \end{aligned} \tag{2.2}$$

This bound is better known as the *evidence lower bound*, or ELBO for short, which we will denote as  $\mathcal{L}(\theta, \phi; \mathbf{x}^{(i)})$ . An interpretation for the terms of the last equation is that the

objective is to have the posterior  $q_\phi(\mathbf{z}|\mathbf{x}^{(i)})$  match the prior  $p(\mathbf{z})$  as accurately as possible while simultaneously maximizing the likelihood of the data point  $\mathbf{x}^{(i)}$  under the model.

In many cases the KL-divergence can be integrated analytically, for instance in the case of two Gaussian distributions. In cases where the KL term cannot be solved analytically, Monte Carlo methods can be used to approximate the expectation.

Several modifications to this objective have been proposed, e.g. the  $\beta$ -VAE [24, 9],  $\beta$ -TCVAE [12] and InfoVAE [81], which aim to improve the learning of better latent representations. Beta-VAE prefixes the KL term with a constant  $\beta$  which is interpreted as a Lagrange multiplier that adjusts the regularization imposed by the latent prior. The case where  $\beta = 1$  corresponds to the VAE formulation presented in this section, while  $\beta > 1$  [Note: more learning pressure to match the prior, for factorized models this corresponds to more "disentanglement".  $\beta$ -TCVAE decomposes the  $\beta$ -VAE loss for factorized models to reveal a correlation term between latent variables which it attempts to penalize. InfoVAE on the other hand attempts to maximize the mutual information between the latent code and the reconstructed output to enforce utilization of the latent code even when flexible decoder distributions are used.]

## Obtaining Differentiable Monte Carlo Estimates

To optimize the parameters  $\theta$  and  $\phi$  of our neural network using backpropagation we require a way to compute the gradient of the expectations of random variables. By introducing a random noise variable as input we are able to obtain samples from the latent distribution by using the *reparameterization trick*.

$$\mathbf{z}^{(i,l)} = g_\phi(\boldsymbol{\epsilon}^{(i,l)}, \mathbf{x}^{(i)}), \boldsymbol{\epsilon}^{(i,l)} \sim p(\boldsymbol{\epsilon})$$

$$\mathbb{E}_{q_\phi(\mathbf{z}|\mathbf{x}^{(i)})}[f(\mathbf{z})] \simeq \frac{1}{L} \sum_{l=1}^L f(g_\phi(\boldsymbol{\epsilon}^{(i,l)}, \mathbf{x}^{(i)}))$$

$$\mathcal{L}(\theta, \phi; \mathbf{x}^{(i)}) = -D_{\text{KL}}(q_\phi(\mathbf{z}|\mathbf{x}^{(i)}) \parallel p(\mathbf{z})) + \frac{1}{L} \sum_{l=1}^L \log p_\theta(\mathbf{x}^{(i)}|\mathbf{z}^{(i,l)})$$

$$\mathcal{L}(\theta, \phi; \mathbf{x}^{(i)}) = \frac{1}{L} \sum_{l=1}^L \left[ q_\phi(\mathbf{z}^{(i,l)}|\mathbf{x}^{(i)}) - p(\mathbf{z}^{(i,l)}) + \log p_\theta(\mathbf{x}^{(i)}|\mathbf{z}^{(i,l)}) \right]$$

## Network Structure

It is important to note that the output  $\hat{\mathbf{x}}^{(i)}$  of the network in Figure 2.5 should not be interpreted as the final reconstruction of the input like in traditional autoencoders, but rather as the values parameterizing the distribution  $p_\theta(\mathbf{x}|\mathbf{z}^{(i,l)})$ .



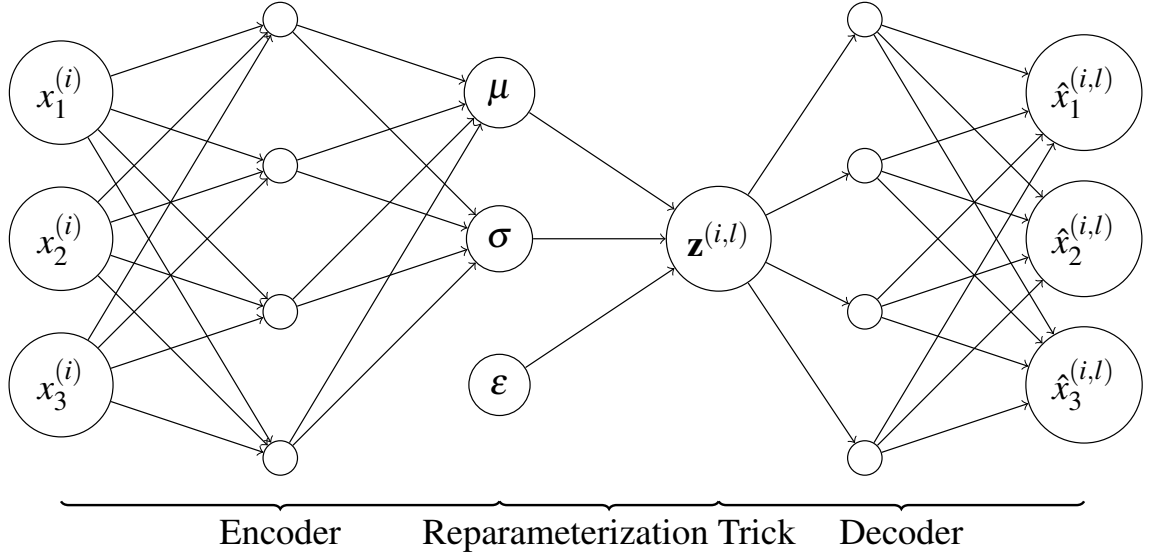


**Figure 2.5.** Variational Autoencoder

[56, 37, 71]

[36, 48]

## 2.2 t-Distributed Stochastic Neighbor Embedding

Taking a slight departure from the preceding discussion on neural networks, the theory, and development leading to the acclaimed dimensionality reduction algorithm t-SNE will be presented. At the end of this section, a way to utilize the t-SNE objective to train an embedding function parameterized by a neural network will be shown, thereby connecting this section with the previous in a natural way, as well as covering the final preliminaries to the contribution of this thesis.

### 2.2.1 SNE

The Stochastic Neighbor Embedding (SNE) algorithm [25], developed by Hinton and Roweis in 2003, serves as the precursor to the later improved t-SNE algorithm. As such, SNE shares many similarities in its definition with t-SNE, and thus by first developing an understanding of SNE and its pitfalls the motivation behind the t-SNE algorithm become more apparent.

[Note: FIXME: As the algorithm's name suggests, the approach SNE takes to perform dimensionality reduction is probabilistic in nature. Without delving directly into the mathematical details, an intuitive overview of the algorithm is that it attempts to embed data points in a lower dimension by preserving probability distributions defining . More concretely, the algorithm proceeds as follows. First, for all data points a probability distribution ... . After these probability distributions have been formed, the actual embedding is

performed by attempting to distribute the points in the output space such that similarly defined probability distributions in the output space match those of the input space as closely as possible. The natural way to match two distributions is familiar from the discussion on variational bayes methods, namely the KL-divergence between the input and output space distributions is used as the objective function for the embedding of data points, which can be optimized with various methods, including the previously covered gradient descent.]

To formalize these notions, we begin with how the conditional probability of data point  $i$  picking data point  $j$  in the input space is defined by the equation

$$p_{j|i} = \frac{\exp(-\|\mathbf{x}_i - \mathbf{x}_j\|^2 / 2\sigma_i^2)}{\sum_{k \neq i} \exp(-\|\mathbf{x}_i - \mathbf{x}_k\|^2 / 2\sigma_i^2)}, \quad (2.3)$$

where the probability can be seen as being derived as if a Gaussian were centered on  $\mathbf{x}_i$  and an appropriate normalizing term is used to scale the individual probabilities so that they sum to 1. The variance (denoted by  $\sigma_i$  in the equation) is determined separately for each data point  $i$  by forcing the perplexity of the conditional distribution over all other data points (later denoted as  $P_i$ ) to equal some preset value.

Perplexity is an information theoretic measure of how well a distribution predicts its samples. For a given probability distribution, perplexity is defined as the exponentiation of the distribution's entropy  $H$ , e.g. in the case of our discrete  $P_i$ :

$$b^{H(P_i)} = b^{-\sum_{j=1}^n p_{j|i} \log_b p_{j|i}},$$

where  $b$  is the unit used to measure entropy, typically chosen to be either 2 or  $e$ , for bits or nats, respectively. From the definition, we can see that larger variance will be chosen for the Gaussians in areas of the input space where the density of data points is low and smaller variance will be used in high density areas. Effectively, variance is adapted to fit the core assumption that the data points lie on a uniformly sampled manifold within the input space. Perplexity is thus a value proportional to the number of effective local neighbors considered by the algorithm when the embedding is being optimized. In practice, the correct  $\sigma_i$  for each  $i$  is numerically sought using the bisection method, up to a small error tolerance in the resulting perplexity.

The conditional distribution in the output space is similarly defined with a Gaussian kernel:

$$q_{j|i} = \frac{\exp(-\|\mathbf{y}_i - \mathbf{y}_j\|^2)}{\sum_{k \neq i} \exp(-\|\mathbf{y}_i - \mathbf{y}_k\|^2)},$$

where each  $\mathbf{y}_i$  represents the point in the embedding for data point  $\mathbf{x}_i$ . A notable difference is the absence of the variance term  $2\sigma_i^2$ , which can be interpreted as having been set to 1

throughout. This choice of fixed variance can, in turn, be interpreted as smoothing out the manifold of the input space when performing the embedding.

Now that we have defined both the output and input distributions for points, the objective function can be formulated as the sum of KL-divergences between each input-output distribution pair:

$$C_{\text{SNE}} = \sum_i D_{\text{KL}}(P_i \parallel Q_i) = \sum_i \sum_{j \neq i} p_{j|i} \log \frac{p_{j|i}}{q_{j|i}}. \quad (2.4)$$

To optimize this objective, gradient descent is typically used to update the positions of the embedded data points. The partial derivative of the objective w.r.t. a point  $i$  in the embedding is given by

$$\frac{\partial C_{\text{SNE}}}{\partial \mathbf{y}_i} = 2 \sum_{j \neq i} (\mathbf{y}_i - \mathbf{y}_j) (p_{j|i} - q_{j|i} + p_{i|j} - q_{i|j}), \quad (2.5)$$

which can be used to form the gradient. This has the intuitive interpretation of a force directed layouting algorithm, where each pair of points is either pushing or pulling on each other, depending on whether they are less or more likely to be neighbors under the output's conditional distribution than the input's.

An important fact to note is that the objective function is in fact non-convex, which implies the unfortunate property that the optimization of the objective function is not guaranteed to terminate at the global optimum due to the potential existence of multiple local minima. One of the main drawbacks of SNE is how it easily ends up in poor local minima. A common way to attempt to avoid poor local minima is to add Gaussian noise to the points in the embedding which is gradually reduced during optimization. This however adds more tunable hyperparameters to the algorithm. In addition to adding this jitter to the embedding points, random restarts are recommended in practice, which become very costly to run when dealing with large data sets.

### 2.2.2 t-SNE

The t-SNE algorithm aims to address two issues of the original SNE algorithm. First, one of the main issues with plain SNE is the so-called *crowding problem*, which is addressed by considering a heavier tailed probability distribution function in the output space, namely the Student's t-Distribution. Second, through considering joint distributions instead of conditional distributions and the use of a different distribution in the output space lead to an objective function that is easier to optimize than that of SNE. Together these improvements

enable better separation of natural clusters in the output space of the algorithm, as compared to the original SNE method.

The crowding problem is named after the phenomenon where distances in a high dimensional space cannot faithfully be modelled in a lower dimensional space, causing the SNE algorithm to collapse points together in the embedding and thus preventing the formation of natural clusters. One can easily verify that it is not possible in the general case to preserve distances perfectly when performing dimensionality reduction, as a space of  $n$  dimensions allows for a maximum of  $n + 1$  equidistant points. How the crowding problem manifests can be seen by considering how the volumes of objects, and by extension the densities of probability distributions, are concentrated in high dimensional space. Unintuitively, as the number of dimensions increase, the concentration of a Gaussian distribution's density shifts from its mean to a shell around its mean [75, p. 50]. When SNE attempts to match probabilities derived from Gaussian kernels in different dimensionalities, moderately distant points in the high dimensional space will have a disproportionately large force attracting them to the center of the lower dimensional kernel. In addition to SNE, the crowding problem is also present in other nonlinear dimensionality reduction methods which are based on preservation of pairwise distances of points, such as Sammon mapping [45].

To address the crowding problem the t-SNE algorithm switches the Gaussian kernels of the output space to ones formed with the Student's t-Distribution. The benefit a t-Distribution has over a Gaussian is that it places more of its probability density in its tails. This property of the distribution allows moderate distances in the input space to be modeled further apart in the output space, alleviating the crowding problem by reducing the attractive forces between moderately distant points and thereby facilitating the formation of more distinct clusters in the embedding. In addition, using a t-Distribution has the computational advantage of not having to perform exponentiation when computing probabilities.

The probability density function of a t-Distribution with  $\nu$  degrees of freedom is given by

$$f(x|\nu) = \frac{\Gamma(\frac{\nu+1}{2})}{\sqrt{\nu\pi} \Gamma(\frac{\nu}{2})} \left(1 + \frac{x^2}{\nu}\right)^{-\frac{\nu+1}{2}},$$

which can be recognized to be closely related to the Gaussian distribution, in fact as  $\nu \rightarrow \infty$  the probability density approaches that of the standard normal distribution. One can observe that the number of degrees of freedom controls how much probability density is placed in the tails of the distribution. The standard choice for t-SNE is to choose  $\nu = 1$  when reducing to a very low number of dimensions, such as 2 or 3 for visualization of a data set as a scatter plot. However, more generally it is suggested to consider higher degrees of freedom when embedding to higher dimensional spaces, as the crowding problem becomes less prominent and thus the required amount of compensation is reduced.

Similarly to Symmetric SNE [14], instead of matching conditional distributions in the input and output spaces, t-SNE forms a joint distribution over all pairs of points in both the

input and output space, which it attempts to match. The joint distribution over the input points is formed by using Equation 2.3:

$$p_{ij} = \frac{p_{j|i} + p_{i|j}}{2N}$$

$$q_{ij} = \frac{(1 + \|\mathbf{y}_i - \mathbf{y}_j\|^2 / \nu)^{-\frac{\nu+1}{2}}}{\sum_{k \neq l} (1 + \|\mathbf{y}_k - \mathbf{y}_l\|^2 / \nu)^{-\frac{\nu+1}{2}}}$$

The t-SNE objective function is defined similarly to the SNE objective (cf. Equation 2.4), except the sum is taken over KL-divergences of the joint probabilities:

$$C_{\text{t-SNE}} = \sum_{i \neq j} p_{ij} \log \frac{p_{ij}}{q_{ij}}.$$

For which the following gradient can be derived:

$$\frac{\partial C_{\text{t-SNE}}}{\partial \mathbf{y}_i} = 4 \sum_{j \neq i} (\mathbf{y}_i - \mathbf{y}_j) (p_{ij} - q_{ij}) (1 + \|\mathbf{y}_i - \mathbf{y}_j\|^2 / \nu)^{-\frac{\nu+1}{2}} \quad (2.6)$$

[Note: Methods to improve the runtime of t-SNE have been subsequently proposed: [80, 44]. Use of the fast multipole method [58] has not been explored due to no suitable multipole expansion for the t-Distributed forces in the output space exist.]

[Note: Worth a mention are the Stochastic Triplet Embedding [72] and Multiple Maps t-SNE [46] methods developed on top of t-SNE, developed to handle non-metric similarities present in the data.]

### 2.2.3 Parametric t-SNE

A major drawback of most nonlinear dimensionality reduction methods is that they do not directly enable out-of-sample extensions.

A natural extension to t-SNE would be to learn a function parameterizing the embedding from input space to output space.

The basic idea behind PTSNE is very straightforward. A feedforward neural network is used to parameterize a function  $f_{\mathbf{W}} : X \mapsto Y$ , which maps points from input space to output space in such a way as to minimize the t-SNE objective. Once the parameters of the mapping are learned, performing dimensionality reduction on any given point is done simply by running it through the neural network.

By application of the chain rule, we can write the gradient w.r.t. the parameters of the neural network as

$$\frac{\partial C_{t\text{-SNE}}}{\partial \mathbf{W}} = \frac{\partial C_{t\text{-SNE}}}{\partial f_{\mathbf{W}}(\mathbf{x}_i)} \frac{\partial f_{\mathbf{W}}(\mathbf{x}_i)}{\partial \mathbf{W}}.$$

As  $f_{\mathbf{W}}(\mathbf{x}_i) = \mathbf{y}_i$ , Equation 2.6 is used to compute the first term of the product, while standard backpropagation can be applied to the rest of the network.

### 3. METHOD

[Note: TODO: go over what this method attempts to improve upon. Other methods are not as scalable, various problems with curse of dimensionality, parametric t-SNE has been previously shown to be slow to optimize and produce poorer results.] [Note: Even though the VAE addresses issues with scalability and reliance on pairwise distances in the input space, the resulting latent code does not allow for as good separation of clusters as other methods, such as t-SNE would, due to the strong effect the imposed prior has on the global shape of the embedding of a data set.]

The method proposed in this work involves combining the VAE model with Parametric t-SNE to produce a general framework for improved parametric dimensionality reduction for data visualization. In this chapter the learning algorithm as well as a variation of it is described.

#### 3.1 Learning a Parametric Embedding Using VAE Sampling

[Note: The aim of the method is to take advantage of the strengths of both VAE and PTSNE.] [Note: Pros of VAE: generative model, stochasticity brings robustness, scalable parametric nonlinear dimensionality reduction] [Note: Pros of PTSNE: theoretically capable of learning as good projections as t-SNE, which is widely considered SOTA. Also scalable and parametric, if trainable with smaller batch sizes.] [Note: Using the notation of the previous chapter, we can summarize the learning procedure as Algorithm 1.]

---

**Algorithm 1** Training of the neural networks.

---

**Input:** Data set  $\mathbf{D}$ .**Output:** Neural network parameters  $\theta, \phi, \mathbf{W}$ 

```

1:  $\theta, \phi, \mathbf{W} \leftarrow$  Initialize parameters
2: while VAE not converged do
3:    $\mathbf{X} \leftarrow$  Random minibatch from  $\mathbf{D}$ 
4:   for all  $\mathbf{x}^{(i)} \in \mathbf{X}$ 
5:      $\epsilon^{(i,l)} \leftarrow$ 
6:      $\mathbf{z}^{(i,l)} \leftarrow g_\phi(\epsilon^{(i,l)}, \mathbf{x}^{(i)})$ 
7:      $\theta, \phi \leftarrow$  Update parameters with  $\nabla_{\theta, \phi} \mathcal{L}$ 
8:   end for
9: end while
10: while PTSNE not converged do
11:    $\mathbf{X} \leftarrow$  Random minibatch
12:    $\hat{\mathbf{x}}^{(i)}$ 
13:    $\mathbf{W} \leftarrow$  Update parameters with  $\mathbf{x}^{(i)}$ 
14: end while

```

---

[Note: After training, a deterministic projection for all subsequent points can be obtained with Algorithm 2.] [Note: For encoder networks that directly parameterize the mean of a distribution, computing the expectation can be done exactly with zero overhead.]

---

**Algorithm 2** Projection.

---

**Input:** Point  $\mathbf{x}$ , neural network parameters  $\theta, \phi, \mathbf{W}$ **Output:** Projected point  $\mathbf{y}$ 

```

1:  $\mathbf{z} \leftarrow \mathbb{E}_{p(\epsilon)}[g_\phi(\epsilon, \mathbf{x})]$ 
2:  $\hat{\mathbf{x}} \leftarrow \mathbb{E}[f(\mathbf{z})]$ 
3:  $\mathbf{y} \leftarrow f_{\mathbf{W}}(\hat{\mathbf{x}})$ 

```

---

### 3.2 Obtaining Reconstructions from Hidden Layers

Instead of training the embedding network on the final output of the observation model it is possible to instead use the outputs of a chosen hidden layer. If the chosen hidden layer has dimensions considerably smaller than that of the original, the benefits of this approach are twofold:

- We are performing a step of nonlinear dimensionality reduction that is not dependent on local distance metrics, i.e. a preprocessing step that is less susceptible to the curse of dimensionality.
- Given that the number of dimensions can be chosen to be considerably lower than in the original input space, computing the t-SNE loss also becomes proportionally cheaper.



When considering precomputed  $P_{ij}$  matrices for each batch the gain in computational advantage does however diminish significantly, although the following caveats apply to the precomputation. Storing the precomputed matrices will require considerable space for large batch sizes and data sets. A way to circumvent the need for large storage space is to employ a k-NN approximation when computing  $P_{ij}$ , i.e. only considering a small number of neighbors when computing the conditional probabilities for each pair of points, which will result in a sparse matrix. This however increases the error in the computed gradient and relies on an efficient k-NN algorithm in practice. Additionally, fixing the batches in advance hinders the performance of SGD as the gradient estimates become biased. Moreover, relying on precomputed  $P_{ij}$  matrices for fixed batches prevents the use of infinite sample generation from the VAE.

### 3.3 Inference with the Generative Model

From the underlying generative model we can approximately compute the marginal  $p(\mathbf{x})$  for each data point  $\mathbf{x}$ . An approximation can be retrieved by importance sampling [57]:

$$p(\mathbf{x}) \simeq \frac{1}{N} \sum_{i=1}^N \frac{p(\mathbf{x}|\mathbf{z}^{(i)})p(\mathbf{z}^{(i)})}{q_{\theta}(\mathbf{z}^{(i)}|\mathbf{x})},$$

where  $\mathbf{z}^{(i)} \sim q_{\theta}(\mathbf{z}|\mathbf{x})$ .

Using the obtained marginals as feedback we can inform the user of potentially anomalous points in the data set. This feedback can then further be used in downstream analysis. From a data visualization perspective points that do not fit the model well correspond to points that are likely to be mapped poorly, thus removing such outliers from the final mapping serves to highlight the natural clusters in the data more clearly.

[Note: discuss the more accurate but computationally costly marginal estimation method: annealed importance sampling [53, 78]?]

[Note: could discuss, experiment with modification to the algorithm: if  $p(\mathbf{x})$  (or even more simply just the reconstruction error) is high (above some threshold), pass the original data point and not the reconstruction to the mapping. This proved to work for the small subset experiment when limiting the latent dimension to  $\leq 3$ . Reason for this being that the VAE trained on only 600 samples poorly reconstructed the test set (basically just corrupting many of them).]

### 3.4 Robustness to Sparse and Noisy Data

### 3.5 Implementation

An accompanying implementation of the method has been made available at <https://github.com/ahie/vptsne>. The implementation is built on top of TensorFlow [1] and takes

advantage of the TensorFlow Distributions [17] library. To take full advantage of the dataflow architecture of TensorFlow and the parallelism provided by GPUs, both the t-SNE loss and its gradient computation were implemented as custom CUDA [54] kernel operations.

The implementation has been made as extensible as possible by allowing the full specification of the neural network structures parameterizing the VAE distributions and the PTSNE network. Helpers for easily specifying common network structures are included in the implementation. The use of normalizing flows in the VAE model has also been made possible. Additionally, the fast approximate nearest neighbor algorithm NN-descent [18] has been included in the t-SNE CUDA routines as an optional performance enhancement for computing the input space distribution  $P$  when training with large batch sizes.

## 4. EXPERIMENTS

[Note: Experiments are carried out to validate the efficacy of the method, as well as compare it to previous methods.] Lastly, two applications of the method to single cell data analysis are presented in sections 4.9 and 4.10.

The code and data used to reproduce all the results presented in this section have been made available at <https://github.com/ahie/vptsne-results>.

### 4.1 Data Sets

To empirically validate the claims of advantageous properties of the proposed method the combined model was studied on the five different data sets described below.

#### 4.1.1 MNIST

The MNIST data set [41] contains labeled images of handwritten digits. Each image contains a single digit in gray-scale with a resolution of 28x28 pixels. The data set is split into 60000 training images and 10000 test images. All networks were trained solely on the training data set, while the remaining test examples were reserved for assessing the capability of the network to generalize to out-of-sample extensions. In the unsupervised setting considered here, the provided labels were only used for visualizing the embeddings and evaluating the embedding quality of out-of-sample extensions via a 1-NN classifier.

MNIST is a standard data set that frequently appears in machine learning literature and is regularly included in unsupervised learning experiments. As a relatively simple labeled real-world data set it functions as a good baseline for studying the output of our method.

#### 4.1.2 Fashion-MNIST

The Fashion-MNIST data set [79] was designed as a drop-in replacement for the MNIST data set and thus contains the same number of grayscale training and test images of equal dimensions. The images themselves consist of 10 different classes of fashion items, such as T-shirts, trousers, sneakers, and handbags. The motivation for considering this data set in addition to MNIST is the fact that it has been shown to be harder to learn even with supervised computer vision methods.

#### 4.1.3 Mass Cytometry

Cytometry is the measurement of biological characteristics of cells. In mass cytometry, time-of-flight mass spectrometry is used to measure the counts of cellular proteins present

within a single cell by tagging proteins with their corresponding antibodies that have been conjugated with specific heavy metals.

As a comparatively new methodological development, mass cytometry enables simultaneous measurement of a considerably greater number of features compared to fluorescence-based flow cytometry. A greater number of features, however, poses new challenges in analyzing the measurement results. To aid the analysis of this high dimensional data it is common to visualize the data as a 2-D or 3-D scatter plot using t-SNE, due to its capability to separate biologically relevant subpopulations of cells in the produced embedding [3]. However, as a high-throughput method, mass cytometry data sets under analysis can grow to be millions of data points in size, prompting the use of more scalable algorithms. For a more thorough review of mass cytometry and associated analytical challenges, the reader is referred to [66].

In our experiments, we consider two different mass cytometry data sets. As the first data set, henceforth referred to as Cytometry A, we use the publicly available data of [42], which has been used to demonstrate the effectiveness of the Phenograph clustering algorithm on mass cytometry data. The data set consists of 81000 data points of 13 dimensions corresponding to the normalized counts of cell surface proteins belonging to distinct clusters of differentiation. As a benchmark data set for the Phenograph clustering algorithm, we additionally include the labels produced by Phenograph in our analysis.

The second mass cytometry data set (Cytometry B) contains data gathered from ovarian cancer patients at different phases of treatment. The number of points in the entire data set is 1.4 million, each of which has 23 dimensions.

#### 4.1.4 Single-Cell RNA Sequencing

Single-cell RNA sequencing (scRNA-seq) enables the measurement of the transcriptional activity within single cells. By counting the number of RNA transcripts present in a given cell matching those of predetermined genes the expression profile of tens of thousands of genes can be measured. As the number of genes for which the strength of expression can be quantified simultaneously is far greater than the number of proteins that can be measured with mass cytometry the computational and analytical challenges are further exacerbated [13, 68].

We explore how our method applied to scRNA-seq data reveals biologically meaningful insights by applying it to the melanoma patient data set studied in [70]. The data set consists of tumor samples from 13 different patients, altogether containing 4097 cells for which the expression of 22462 genes is measured. The data set additionally includes labels for each cell denoting their cell type and tumor of origin.

## 4.2 Evaluation Metrics

To quantitatively evaluate the quality of embeddings two different measures are used in this work. By quality of the embeddings we are interested in how well the local structure of the data is preserved. The choice of the two metrics used in this work follows those used in the original parametric t-SNE paper [43]. A short description for each is given below.

### 4.2.1 k-Nearest Neighbor Classifier

Given a labeled data set a k-nearest neighbor (k-NN) classifier can be used to roughly assess how well different classes are separated in the output space of an embedding. A k-NN classifier works simply by returning the majority label of a given point's k-nearest neighbors in the training data set. For example in the 1-NN classifier case, the decision boundary can be geometrically visualized as a Voronoi diagram as in Figure 4.1.

Throughout the experiments, the performance of nearest neighbor classifiers in the output space of embeddings will be evaluated. More precisely, the accuracy of a 1-nearest neighbor classifier with the Euclidean metric for determining neighbor distance is used.

For parametric methods, the classifier can be trained on the embedding of training data points and separately tested on the training set. This enables evaluating the ability of the embedding function to generalize to unseen data. On the other hand, for non-parametric methods, the final embedded data points need to be split into train and test sets for the 1-NN classifier.

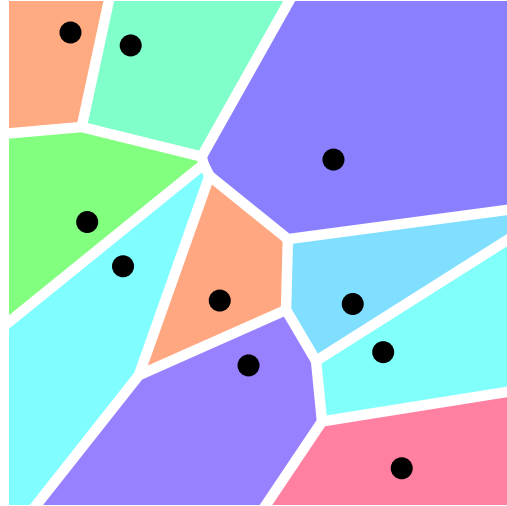


**Figure 4.1.** Voronoi diagram illustrating the decision boundaries of 10 different classes of a 1-NN classifier. Black dots represent the training data points, and the different colors correspond to the label of the data point for that region. Any point to be classified would receive the label corresponding to the location in the tessellation it lies on. The distance metric used in this example is the Euclidean distance.

### 4.2.2 Trustworthiness

Trustworthiness, introduced by Venna et al. [73], is a measure of the degree to which local structure is preserved in the output space relative to the input space after dimensionality reduction is performed. Trustworthiness has been used to compare multiple dimensionality reduction methods for the purposes of visualization of high dimensional data sets such as gene expression data [33] and gene interaction graphs [74].

Computation of trustworthiness is done by comparing how the rank order for each point's  $k$  nearest neighbors in the output space match that of the input space. Formally, for a chosen number  $k$  of neighbors it is given by the following

$$T(k) = 1 - \frac{2}{nk(2n - 3k - 1)} \sum_{i=1}^n \sum_{j \in \mathcal{N}_i^k} (r(i, j) - k),$$

where  $n$  is the total number of data points under consideration,  $\mathcal{N}_i^k$  is the set of  $k$  nearest neighbors in the output space of data point  $i$ , and  $r(i, j)$  is a function giving the rank of node  $j$  in the nearest neighbor ordering of node  $i$ . The possible values for trustworthiness range from 0 to 1, indicating complete loss of local structure and perfect preservation of local structure, respectively.

## 4.3 Network Structure and Parameters

To parameterize the embedding  $f(\hat{\mathbf{x}})$  a feedforward neural network with layers of hidden units with dimensions  $d - 500 - 500 - 2000 - 2$  were used, where  $d$  is the input dimensionality and rectifier linear unit (ReLU) activations are applied to the hidden unit outputs to induce nonlinearity to the network. The hidden unit dimensions were chosen to match those of the final combined network used in [43], although we have substituted the sigmoid activations with ReLU activations. Furthermore, we do not perform stacked restricted Boltzmann machine pretraining on the hidden layer weights as in [43]. However we do benchmark the performance of our network against the original parametric t-SNE implementation. Since we are not considering RBM pretraining and are instead relying on the property of ReLUs reducing the vanishing gradient problem [21] and better initialization [20]. Running the original implementation shows little benefit in performing this costly initialization. We could instead reuse the trained encoder weights of the VAE as a starting point for the optimization of our embedding network.

For optimization of the neural network [43] use nonlinear conjugate gradient descent, whereas Adam [35] is used as the optimizer in the results presented here. Updates with Adam are considerably faster to compute than with conjugate gradient descent. Throughout all experiments standard parameters for Adam were chosen, i.e. a learning rate of 0.001 and the exponential decay rates of the 1st and 2nd moments were set to 0.9 and 0.999 respectively. The more recent optimizer AMSGrad [55] was considered, but due to little

evidence of its benefit over Adam when used in non-synthetic optimization problems its use was left for future work.

We applied batch normalization [30] to the hidden layers of the VAE networks, while omitting batch normalization from the embedding network. This is to validate the training procedure on as simple an embedding network as possible. We note that applying batch normalization to the embedding network improves the results marginally.

To further emphasize the universality of our approach we restrict ourselves to use a simple VAE structure, without complicating the model architecture with more recently proposed advances, such as normalizing flows [56] ([Note: could show that better models improve performance in the supplement]). Throughout all experiments, unless otherwise specified, the VAE architecture was fixed to  $d - 256 - 128 - 32 - \mu, \log \sigma^2 - 32 - 128 - 256 - d$ , where  $\mu$  and  $\sigma$  parameterize a normal distribution acting as the posterior  $q_\phi(\mathbf{z}|\mathbf{x}^{(i)})$  and the final layer output was used to parameterize a Bernoulli distribution for MNIST as well as Fashion-MNIST, and a Gaussian distribution with a fixed standard deviation of 0.1 for cytometry data. In all experiments, each VAE was trained with a batch size of 1000 for 10000 iterations and had a latent dimensionality of 3, unless otherwise specified.

For MNIST and Fashion-MNIST perplexities were set to 30, which is in line with the value used by [43], whereas for the mass cytometry and scRNA-seq data sets a perplexity of 10 was chosen. It should be noted that a more correct way to choose perplexity would take into account the batch size, as perplexity controls the number of neighbors each point is considered to have. For example training VPTSNE on MNIST with batch size 200 and perplexity 10 gives far better results than with perplexity 30. However, with PTSNE the results are actually worse as the training fails to converge even with small learning rates. An example embedding of MNIST with low perplexity and small batch size has been included in Appendix A, which achieves better trustworthiness (0.935) and 1-NN (0.812) than the 600 batch size, 30 perplexity runs. Why PTSNE fails to converge and VPTSNE does not is an important question to explore in future work, as this demonstrates a clear advantage of the method being proposed.

Degrees of freedom of the t-Distribution for the PTSNE objective was set to 1 throughout all experiments, as all embeddings performed were two-dimensional.

## 4.4 Learning

In this section we compare the effect of training on VAE reconstructions to training on the original MNIST data set. To quantitatively evaluate the quality of the embeddings produced we employed the trustworthiness metric [73] on the MNIST test set. Additionally, we compared the 1-NN classification errors by fitting the classifiers on the produced embeddings of the training set and finding the mean accuracies of the classifiers on the test set.

In figure 4.2 we have plotted the 1-NN scores and trustworthiness of the embeddings obtained after each iteration of training for two different batch sizes. The runs for each batch size were repeated 20 times, plotting the means and 95% confidence intervals. Training with VAE reconstructions shows a clear improvement both qualitatively and quantitatively over training on the original data when small training batches are used to approximate the t-SNE loss gradient. Higher trustworthiness, as well as 1-NN scores are obtained consistently and convergence is reached with far fewer iterations. Moreover, the results are in favor of training on reconstructions by exhibiting more stable results during training.

Qualitatively the embeddings trained on the original data remain noisier than the embeddings trained on the reconstructed data points. This can be seen in figure 4.3, where the separation of true clusters in the embedding is far less evident, with several classes overlapping and a large number of outlier points for each class. We further compare the qualitative differences of the embeddings produced with the Fashion-MNIST dataset. In figure 4.4 similar deficiencies in the embedding can be noted as in the embedding comparisons for the MNIST data set. In particular, the visible clusters of classes are less distinct, as well as the global layout of the classes is considerably worse, e.g. the cluster of footwear related images has been pulled closer to the cluster of upper body garments and the images of bags have been split into two seemingly unrelated clusters.

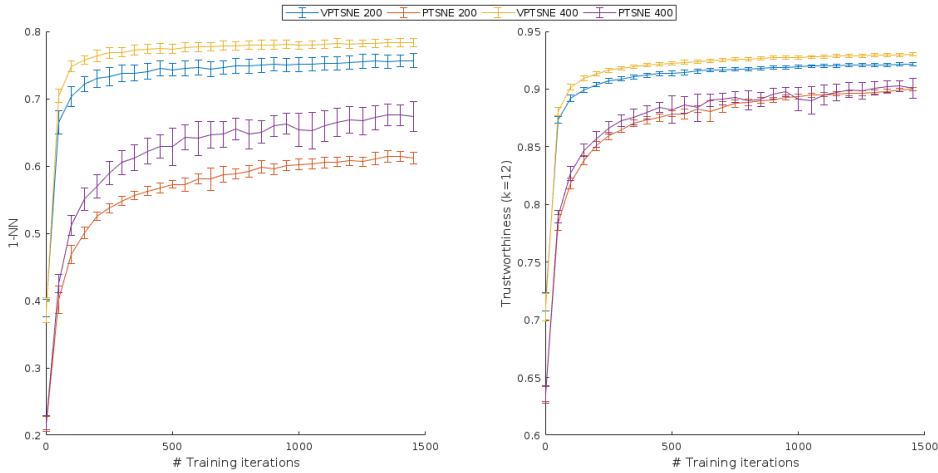


**Figure 4.2.** Plots of 1-NN and trustworthiness scores obtained after a given number of iterations for different batch sizes. The means and 95% confidence intervals have been plotted from 20 repeated runs for each parameter setting.

## 4.5 Comparisons

We now compare the proposed method to other parametric dimensionality reduction methods, namely PCA and VAE. In addition we also consider two non-parametric dimensionality reduction methods, t-SNE and the recently proposed method UMAP [50], which had been demonstrated to be able to produce embeddings comparable to t-SNE while being



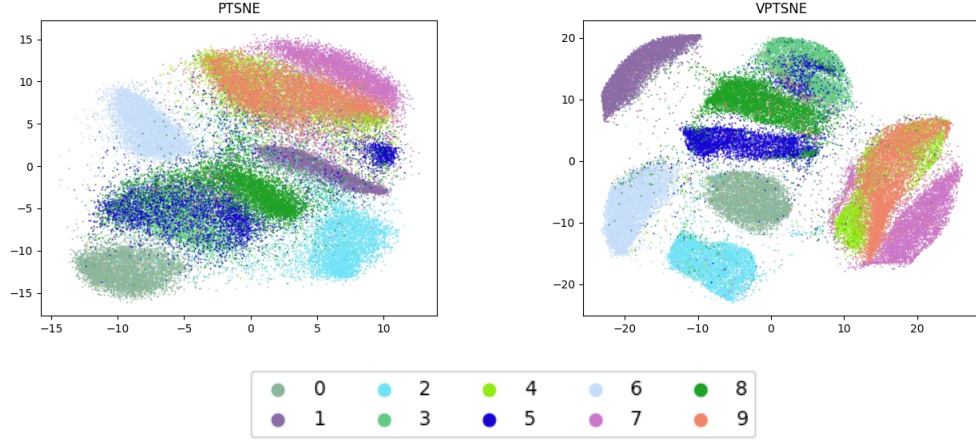


**Figure 4.3.** Embeddings of the MNIST data set trained with batch size 400.

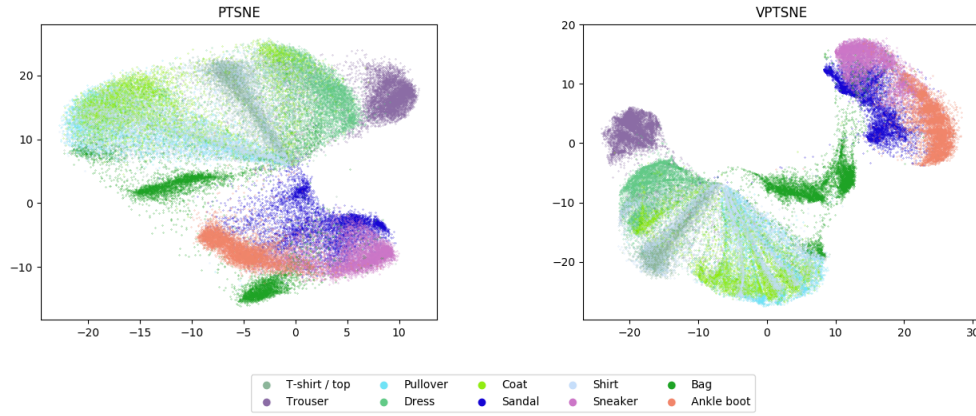


**Figure 4.4.** Embeddings of the Fashion-MNIST data set trained with batch size 400. *[Note: could include UMAP embedding of this data set here for comparison. It is remarkably similar and this would reinforce the claim that small batch size training is actually very effective.]*

more efficient to optimize in practice.

For the comparisons we will be using the Cytometry A data set. As evaluation criteria, similarly to the previous section, both trustworthiness and 1-NN classification accuracy are used. In addition to comparing the quality of the embeddings, the runtime performance of the different methods are studied. Our goal is to demonstrate that our method produces competitive embeddings as well as has superior scalability.

### 4.5.1 Embedding Quality

The quantitative results for all methods under comparison are available in table 4.1 and the corresponding scatter plots of the 2-D embeddings are presented in figure 4.5. Although VAE produces quantitatively better results for the chosen metrics, the spatial layout of clusters in the resulting embedding have less distinct separation and the global structure

of the embedding is constrained by the chosen prior  $p(\mathbf{z})$ . From a data visualization standpoint these factors make the latent space embeddings qualitatively worse than what the corresponding quantitative metrics would suggest. Unsurprisingly, PCA performs the worst on both quantitative and qualitative results. Our method however is able to reach results on par with those of the chosen non-parametric methods.

[Note: The effect of choosing a suitable perplexity w.r.t. batch size mentioned in a previous note is highlighted in 4.5. With large perplexity the clusters in the t-SNE embedding begin to separate more distinctly like with VPTSNE/UMAP, but here the same perplexity is used for both VPTSNE and t-SNE optimization. As perplexity is increased t-SNE optimization becomes considerably slower (for example going from perplexity 10 to 100 increased the total computation time twofold).]

It can also be observed that t-SNE, with the given perplexity, preserves global structure much more poorly. This can be observed by comparing with the PCA plot, which has three clearly distinct, spatially separated clusters of clusters that are not present in the t-SNE plot.

## 4.5.2 Scalability

A major practical challenge with nonlinear dimensionality reduction methods are their scalability to large data sets. Typically, to capture the spatial structure of data a distance metric is employed to compute the pairwise distances for the entire data set, after which a projection of the points to a lower dimensional space, equipped with a corresponding metric, is sought that retains the computed distances as accurately as possible. As the number of data points increases, the inherent quadratic complexity of methods relying on such pairwise distance computations quickly renders such methods intractable.

In practice, various approximations and data structures are employed to speed up dimensionality reduction methods. With t-SNE a widely used performance enhancement, independently investigated by Yang et al. [80] and van der Maaten [44], is to use the Barnes-Hut algorithm [5] to approximate the  $Q_{ij}$  matrix by averaging the influence of distant points belonging to the same node in the underlying space partitioning data structure. This approximation nevertheless fails to provide significant speedup in the general case depending on the chosen tradeoff between accuracy and speed, as well as the distribution of the points being optimized at each step. Furthermore, its use is limited to obtaining 2 or 3 dimensional embeddings due to its use of the quadtree and octree data structures for each respective dimensionality. On the other hand, optimization of the parametric embedding can be performed with stochastic gradient descent. As we have shown, even with small batch sizes we are able to produce embeddings of competitive quality. The Barnes-Hut approximation can also be used to further speed up the computation of the loss and its gradient, but for small batch sizes the computational overhead of constructing the required data structure can outweigh the cost of directly computing all pairwise influences within

**Table 4.1.** Comparison between different dimensionality reduction methods.

Algorithm	Trustworthiness ( $k = 12$ )	1-NN	time (ms)
VPTSNE	0.9753	0.9250	60766
PTSNE	0.9628	0.8890	8729
UMAP	0.9688	0.9297	74716
VAE	0.9762	0.9247	52037
t-SNE	0.9879	0.9536	1192812
PCA	0.8557	0.4886	96

the batch. Direct computation has the additional benefit that it is not limited to output dimensionalities for which a space partitioning data structure can be efficiently built.

As previously mentioned, one of the strengths of UMAP compared to t-SNE is the efficiency of its optimization. The key to its efficient optimization is that its gradient can be approximated stochastically via probabilistic edge sampling following the procedure introduced in [69]. As both VPTSNE and UMAP take advantage of stochastic gradient descent, the scalability of their optimization is equal up to an implementation dependent constant factor. VPTSNE however maintains the advantage over UMAP that natural out-of-sample extension is made possible through the learned embedding function.

## 4.6 Robustness to Sparse Data

As discussed in section [todo and ref. the correct section in methods] the probabilistic model is advantageous when only few data points are available. To show this effect in practice we trained mappings with and without the use of our method on randomly chosen subsets of the MNIST training data set, effectively simulating sparsity of available training data. Evaluation of the mappings was carried out on the full MNIST test set as in previous experiments. A line plot of the obtained scores corresponding to the chosen size of the subsets can be found in figure 4.6. Significant differences in the obtained scores are noted in favor of our method. From these results we can observe that both the trustworthiness and 1-NN scores remain higher even with extremely small data sets, indicating that the use of our method is able to provide better generalization even when few training data points are available.

## 4.7 Robustness to Noisy Data

As real-world data is generally not perfectly clean, an important property for any machine learning method is its capability to handle data containing artifacts. Considering VAEs are inherently robust to corrupted data due to the regularization provided by the stochastic latent code ([should be discussed in a previous section more thoroughly, connection with VAE and Robust PCA [10, 11] shown in [15]]) it is reasonable to hypothesize that a training procedure for a low dimensional mapping taking advantage of this property would perform better on corrupted data.

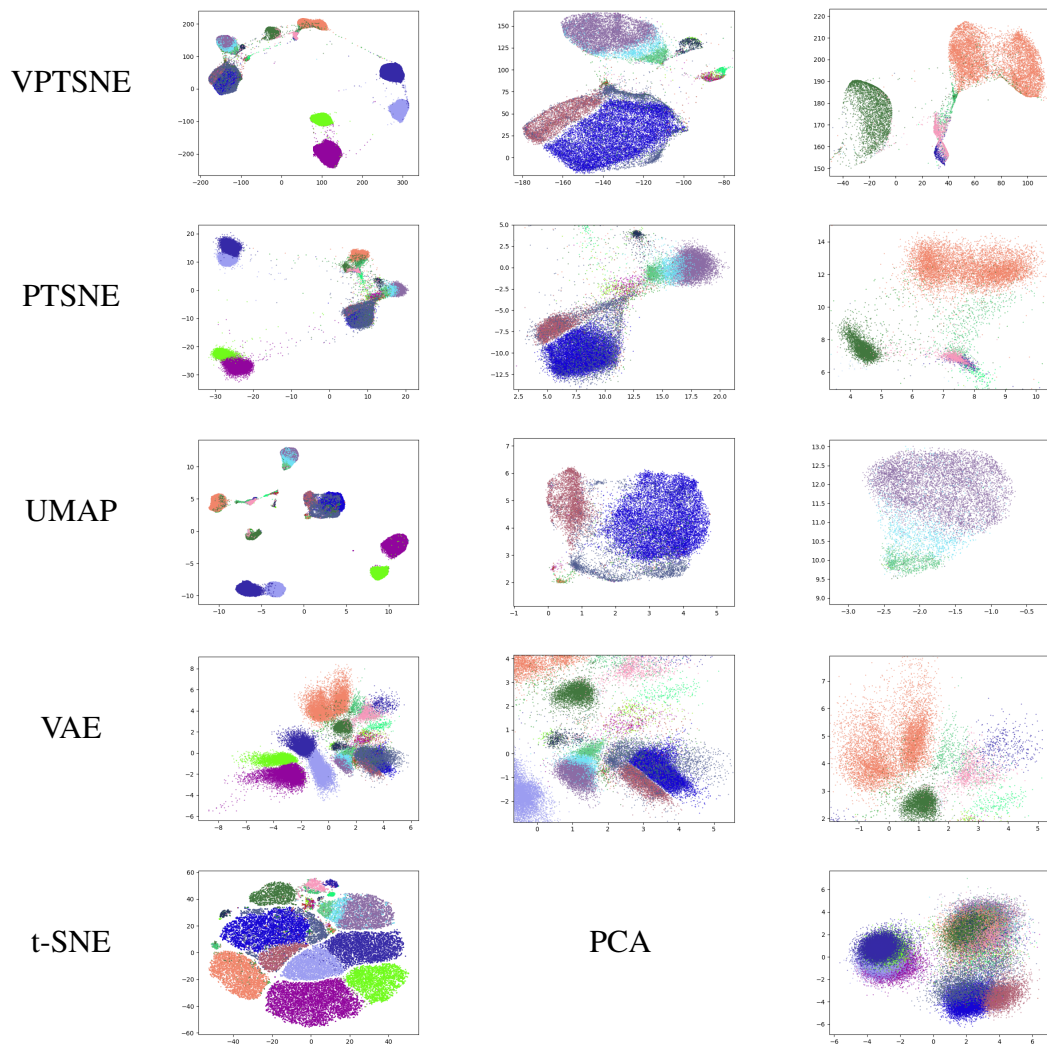


**Figure 4.5.** Cytometry A data set embedded with the methods being compared in section 4.5.

Here we aim to back up this hypothesis by running experiments on artificially corrupted MNIST data sets. As the corruption process in our experiments we consider *masking noise* as in [76], where a predetermined fraction of randomly chosen elements of a data point are set to 0. We test robustness by applying masking noise to 10%, 20%, 30% and 40% fractions of the training and test sets. The results of our experiments (cf. figure 4.7) show a clear advantage to using our method when dealing with noisy data as both evaluation metrics can be observed to decrease considerably for PTSNE as the training data is progressively corrupted, whereas VPTSNE maintains its performance throughout the experiments.

As an example of real-world data corrupted in this fashion, in scRNA-seq so-called *dropout events*, which cause incomplete sequence data to be captured due to technical and biological noise, can be viewed as a form of masking noise. The results presented here would indicate that the proposed method is potentially a good fit for exploratory analysis of scRNA-seq data.

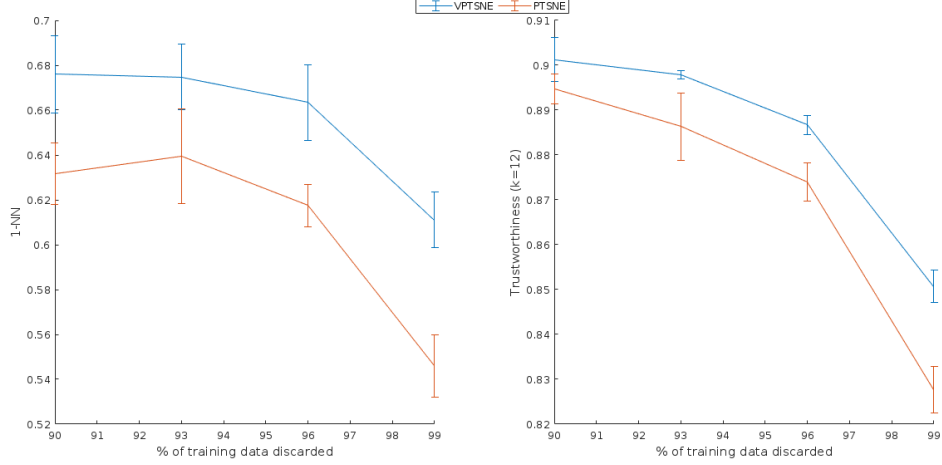


**Figure 4.6.** 1-NN and trustworthiness scores obtained for PTSNE and VPTSNE trained on small subsets of the MNIST data set. Error bars indicate the 95% confidence intervals of the mean for each sparsity level, obtained from 20 repeated runs.

Even with the standard VAE structure, the obtained results are encouraging. As future work it would be interesting to test whether making use of denoising variational autoencoders [29], which are an extension of denoising autoencoders [76] that are directly trained to correct corrupted data. Additionally of interest is how our method fares when other corruption processes are present.

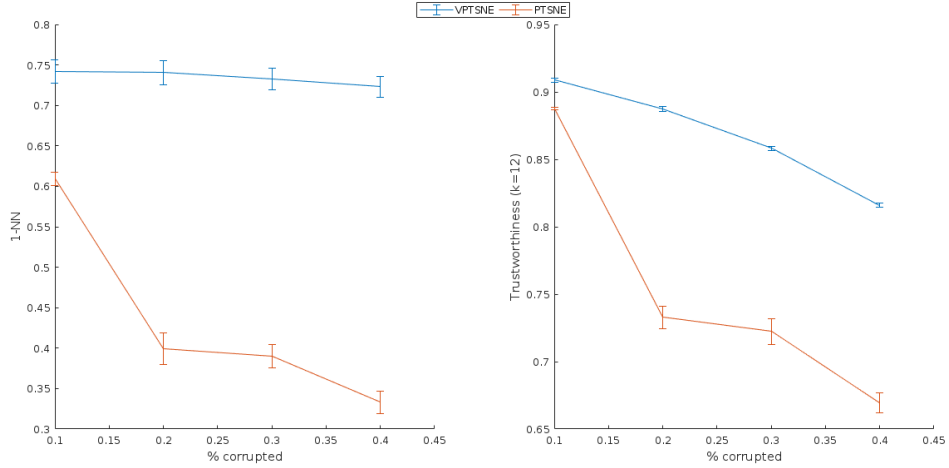


**Figure 4.7.** 1-NN and trustworthiness scores obtained for PTSNE and VPTSNE trained on MNIST data with different levels of masking noise applied. Error bars indicate the 95% confidence intervals of the mean for each corruption level, obtained from 20 repeated runs.

## 4.8 Obtaining Reconstructions from Hidden Layers

To show the efficacy of this modification to the learning procedure we train an embedding using the latent code directly. As we choose the dimensionality of the latent code to be more than two orders of magnitude smaller than that of the original data's it is possible

for us to use batches of far greater size to train the embedding network, without incurring additional computation cost over training with smaller batches on data of the original dimensionality. The latent dimensionality of the VAE was chosen to be 7 and the batch size for training the embedding was set to 5000, as in the original parametric t-SNE paper [43]. The choice of 7 as the VAE latent dimensionality was deliberately made so that it would correspond to the largest number which is two orders of magnitude smaller than the original dimensionality. We have additionally included the embedding of data points obtained with the original implementation of parametric t-SNE for comparison in figure 4.8. Qualitatively and quantitatively an overall better embedding is achieved with less computation using our method.

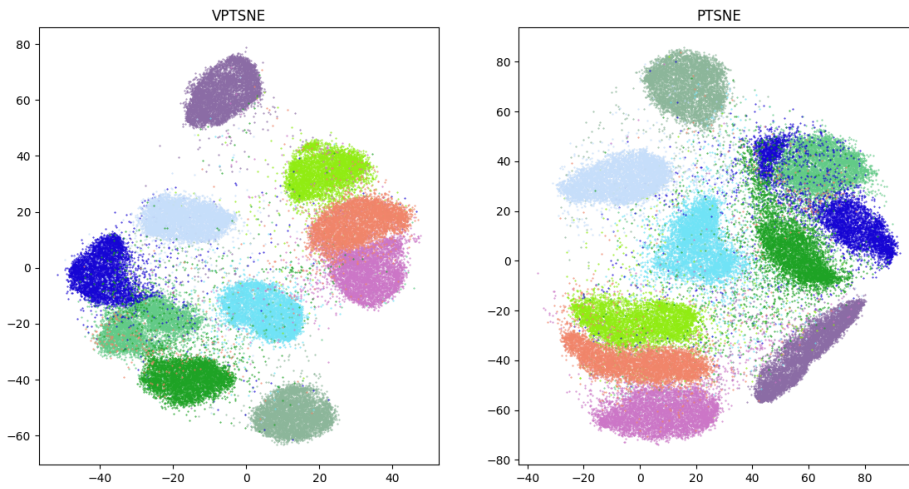


**Figure 4.8.** Embedding produced by training on a 7 dimensional latent representation of the MNIST data set contrasted with the result of the original PTSNE implementation. VPTSNE trustworthiness: 0.927, 1-NN: 0.910. PTSNE trustworthiness: 0.926, 1-NN 0.887.

## 4.9 Inference with the Generative Model

As an example of inference with the generative model discussed in 4.9 we use the Cytometry B data set to train our combined model with two patients' data held out. The protein expression profile of Patient A's cells closely match that of other patients' in the training set, whereas Patient B's sample is from advanced cancer making it an outlier in relation to the data available during training.

To distinguish between outlier and inlier points in the obtained mapping we set a hard threshold of  $\log p(\mathbf{x}) < -150$  to separate between the two. In figure 4.9 embeddings with both patient specific labeling and labeling obtained by thresholding are shown side by side. The high tumor purity sample of Patient B has almost completely been mapped to a small region corresponding to protein expression levels of cancer cells, whereas Patient A's mapping contains several distinct clusters of various cell types. Further, the labels obtained



through thresholding indicate that the majority of cells in Patient B’s sample are indeed considered as outliers by the model, in addition to a handful of visually poorly mapped points.

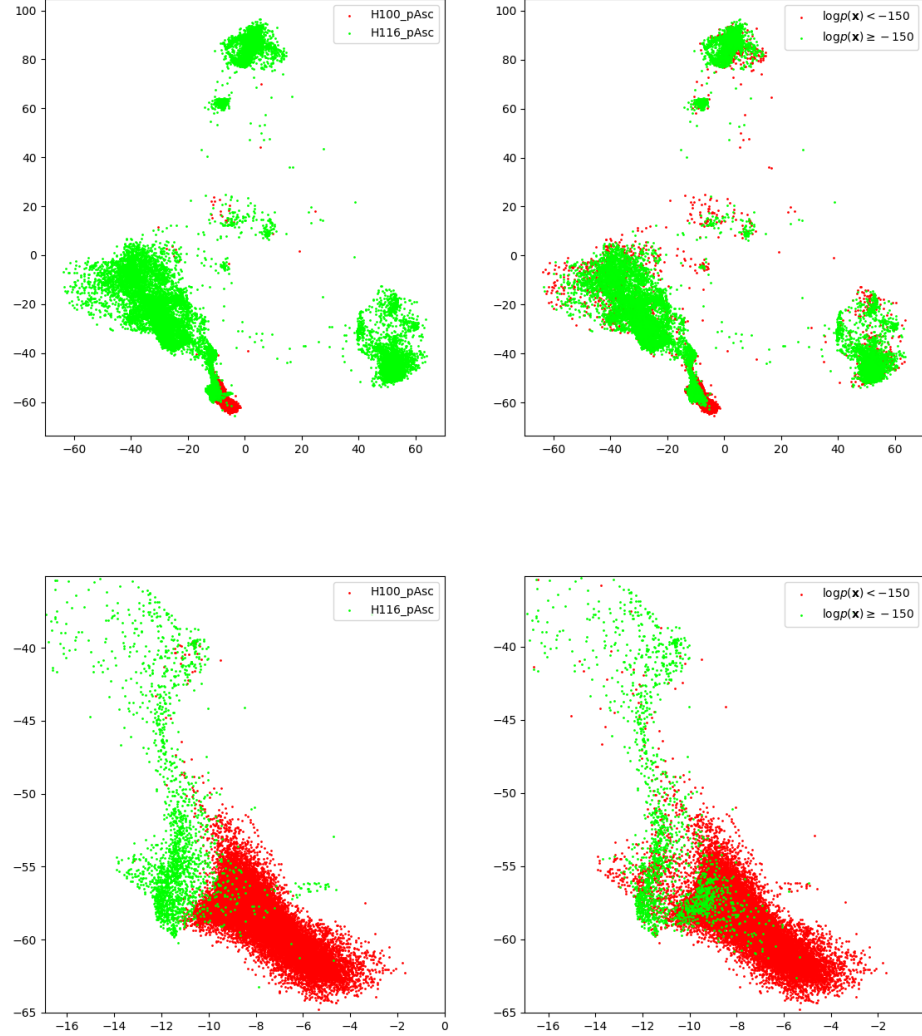


**Figure 4.9.** Detecting outliers in cytometry data. *[Rename patients to match text.]*

## 4.10 Application to scRNA-seq Data

Noting the results presented in the previous sections, we finally aim to demonstrate the applicability of our method to a real-world data set that is both sparse and very high dimensional, as well as contains corruption due to technical variation. For this purpose the scRNA-seq data set of [70] was chosen.

Due to the very high dimensionality in comparison to the other data sets, more capacity to the VAE network was added. The layer dimensions for the VAE architecture were chosen to be  $d - 1000 - 1000 - 500 - \mu, \log \sigma^2 - 500 - 1000 - 1000 - d$  and 50 was chosen as

the latent dimensionality. To train the embedding we used the method of obtaining the reconstructed data points directly from the latent code.

In Figure 4.10 we have visualized the data of [70] using our method and the results of the analysis carried out in the study.

From the results we can see that different tumor samples and cell types cluster well in the embedding. The separation of malignant cells from different patients to separate clusters reveals the heterogeneity of melanoma present in the different tumor samples.

For each cell in the data set so called MITF- and AXL-program scores were computed from the relative expression levels of their corresponding gene sets. These scores aim to provide insight into the potential drug resistance mechanisms of malignant cells. In our embedding a clear gradient from high to low MITF- and AXL-program scores can be seen within the cluster of tumor cell clusters, further indicating that our method is able to highlight biologically meaningful variations in the data.

Cell cycle analysis also reveals the presence of subclusters of cycling cells in our embedding. Cycling cells being cells which are undergoing cell division. The color gradient in the projection for cycling cells corresponds to the strength of the signal indicating cell cycling. Below a given threshold value for this signal, cells were classified as non-cycling.

With such a high dimensional data set, the effect of the curse of dimensionality can be seen on methods based on distances, leading them to produce inferior embeddings. For example, applying UMAP directly to the high dimensional data one of the most obvious shortcomings of the embedding is its failure to distinguish between T- and B-cells. A figure of the UMAP embedding is included in Appendix B for comparison.



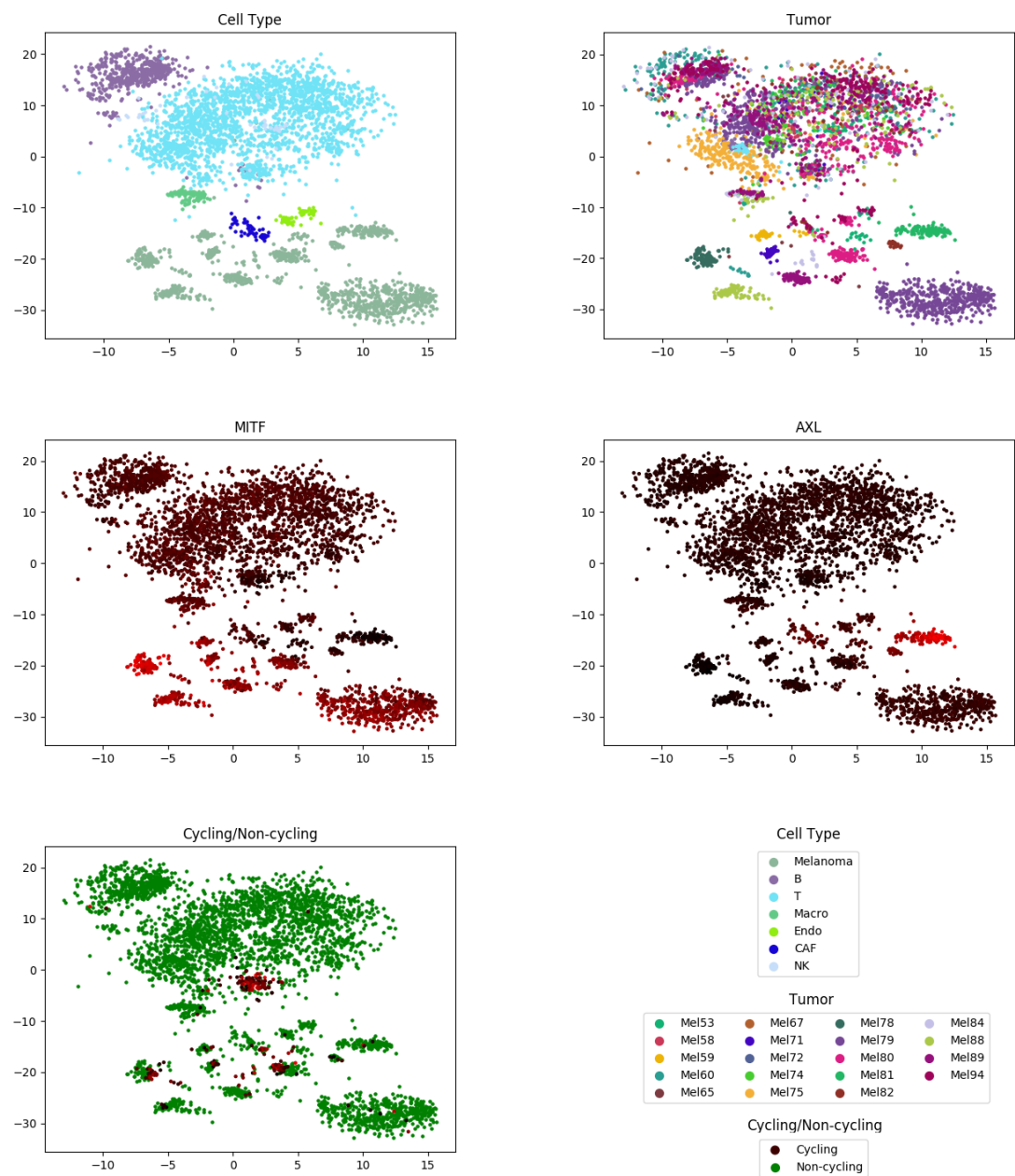


**Figure 4.10.** Visualization of analysis results on data from [70] using VPTSNE.

## **5. CONCLUSIONS**

## REFERENCES

- [1] M. Abadi, P. Barham, J. Chen, Z. Chen, A. Davis, J. Dean, M. Devin, S. Ghemawat, G. Irving, M. Isard *et al.*, Tensorflow: a system for large-scale machine learning., in: OSDI, 2016, Vol. 16, pp. 265–283.
- [2] C.C. Aggarwal, A. Hinneburg, D.A. Keim, On the surprising behavior of distance metrics in high dimensional space, in: International conference on database theory, Springer, 2001, pp. 420–434.
- [3] Amir El-ad David, Davis Kara L, Tadmor Michelle D, Simonds Erin F, Levine Jacob H, Bendall Sean C, Shenfeld Daniel K, Krishnaswamy Smita, Nolan Garry P, Pe'er Dana, viSNE enables visualization of high dimensional single-cell data and reveals phenotypic heterogeneity of leukemia, Nature biotechnology, Vol. 31, Iss. 6, may, 2013, p. 545–552.
- [4] P. Baldi, K. Hornik, Neural networks and principal component analysis: Learning from examples without local minima, Neural networks, Vol. 2, Iss. 1, 1989, pp. 53–58.
- [5] Barnes Josh, Hut Piet, A hierarchical  $O(N \log N)$  force-calculation algorithm, Nature, Vol. 324, dec, 1986, p. 446.
- [6] R.E. Bellman, Dynamic Programming, Princeton University Press, 1957.
- [7] D.M. Blei, A. Kucukelbir, J.D. McAuliffe, Variational inference: A review for statisticians, Journal of the American Statistical Association, Vol. 112, Iss. 518, 2017, pp. 859–877.
- [8] C.J.C. Burges, Dimension reduction: A guided tour, Foundations and Trends® in Machine Learning, Vol. 2, Iss. 4, 2010, pp. 275–365.
- [9] C.P. Burgess, I. Higgins, A. Pal, L. Matthey, N. Watters, G. Desjardins, A. Lerchner, Understanding disentangling in  $\beta$ -VAE, ArXiv e-prints, Apr. 2018.
- [10] E.J. Candès, X. Li, Y. Ma, J. Wright, Robust principal component analysis?, Journal of the ACM (JACM), Vol. 58, Iss. 3, 2011, p. 11.
- [11] V. Chandrasekaran, S. Sanghavi, P.A. Parrilo, A.S. Willsky, Rank-sparsity incoherence for matrix decomposition, SIAM Journal on Optimization, Vol. 21, Iss. 2, 2011, pp. 572–596.

- [12] T.Q. Chen, X. Li, R. Grosse, D. Duvenaud, Isolating sources of disentanglement in variational autoencoders, arXiv preprint arXiv:1802.04942, 2018.
- [13] Clarke Robert, Ressom Habtom W., Wang Antai, Xuan Jianhua, Liu Minetta C., Gehan Edmund A., Wang Yue, The properties of high-dimensional data spaces: implications for exploring gene and protein expression data, *Nature Reviews Cancer*, Vol. 8, jan, 2008, p. 37.
- [14] J. Cook, I. Sutskever, A. Mnih, G. Hinton, Visualizing similarity data with a mixture of maps, in: *Artificial Intelligence and Statistics*, 2007, pp. 67–74.
- [15] B. Dai, Y. Wang, J. Aston, G. Hua, D. Wipf, Connections with robust pca and the role of emergent sparsity in variational autoencoder models, *Journal of Machine Learning Research*, Vol. 19, Iss. 41, 2018, pp. 1–42.
- [16] J. Deng, W. Dong, R. Socher, L.J. Li, K. Li, L. Fei-Fei, Imagenet: A large-scale hierarchical image database, in: *Computer Vision and Pattern Recognition*, 2009. CVPR 2009. IEEE Conference on, Ieee, 2009, pp. 248–255.
- [17] J.V. Dillon, I. Langmore, D. Tran, E. Brevdo, S. Vasudevan, D. Moore, B. Patton, A. Alemi, M. Hoffman, R.A. Saurous, Tensorflow distributions, arXiv preprint arXiv:1711.10604, 2017.
- [18] W. Dong, C. Moses, K. Li, Efficient k-nearest neighbor graph construction for generic similarity measures, in: *Proceedings of the 20th international conference on World wide web*, ACM, 2011, pp. 577–586.
- [19] K.P. F.R.S., LIII. On lines and planes of closest fit to systems of points in space, *The London, Edinburgh, and Dublin Philosophical Magazine and Journal of Science*, Vol. 2, Iss. 11, 1901, pp. 559–572.
- [20] X. Glorot, Y. Bengio, Understanding the difficulty of training deep feedforward neural networks, in: Teh, Y.W., Titterington, M. (eds.), *Proceedings of the Thirteenth International Conference on Artificial Intelligence and Statistics*, Chia Laguna Resort, Sardinia, Italy, 13–15 May, 2010, *Proceedings of Machine Learning Research* 9, PMLR, pp. 249–256.
- [21] X. Glorot, A. Bordes, Y. Bengio, Deep sparse rectifier neural networks, in: *JMLR W&CP: Proceedings of the Fourteenth International Conference on Artificial Intelligence and Statistics (AISTATS 2011)*, Apr. 2011.
- [22] I. Goodfellow, Y. Bengio, A. Courville, *Deep Learning*, MIT Press, 2016. <http://www.deeplearningbook.org>.
- [23] K. He, X. Zhang, S. Ren, J. Sun, Deep residual learning for image recognition, in: *Proceedings of the IEEE conference on computer vision and pattern recognition*, 2016, pp. 770–778.

- [24] I. Higgins, L. Matthey, A. Pal, C. Burgess, X. Glorot, M. Botvinick, S. Mohamed, A. Lerchner, beta-vae: Learning basic visual concepts with a constrained variational framework, 2016.
- [25] G.E. Hinton, S.T. Roweis, Stochastic neighbor embedding, in: Advances in neural information processing systems, 2003, pp. 857–864.
- [26] G.E. Hinton, R.R. Salakhutdinov, Reducing the dimensionality of data with neural networks, science, Vol. 313, Iss. 5786, 2006, pp. 504–507.
- [27] K. Hornik, Approximation capabilities of multilayer feedforward networks, Neural networks, Vol. 4, Iss. 2, 1991, pp. 251–257.
- [28] H. Hotelling, Relations between two sets of variates, Biometrika, Vol. 28, Iss. 3/4, 1936, pp. 321–377.
- [29] D.J. Im, S. Ahn, R. Memisevic, Y. Bengio, Denoising criterion for variational auto-encoding framework, in: Proceedings of the Thirty-First AAAI Conference on Artificial Intelligence, February 4-9, 2017, San Francisco, California, USA., 2017, pp. 2059–2065.
- [30] S. Ioffe, C. Szegedy, Batch normalization: Accelerating deep network training by reducing internal covariate shift, CoRR, Vol. abs/1502.03167, 2015.
- [31] W.B. Johnson, J. Lindenstrauss, Extensions of lipschitz mappings into a hilbert space, Contemporary mathematics, Vol. 26, Iss. 189-206, 1984, p. 1.
- [32] N.P. Jouppi, C. Young, N. Patil, D. Patterson, G. Agrawal, R. Bajwa, S. Bates, S. Bhatia, N. Boden, A. Borchers *et al.*, In-datacenter performance analysis of a tensor processing unit, in: Computer Architecture (ISCA), 2017 ACM/IEEE 44th Annual International Symposium on, IEEE, 2017, pp. 1–12.
- [33] S. Kaski, J. Nikkilä, M. Oja, J. Venna, P. Törönen, E. Castrén, Trustworthiness and metrics in visualizing similarity of gene expression, BMC Bioinformatics, Vol. 4, Iss. 1, Oct, 2003, p. 48.
- [34] N.S. Keskar, D. Mudigere, J. Nocedal, M. Smelyanskiy, P.T.P. Tang, On large-batch training for deep learning: Generalization gap and sharp minima, in: International Conference on Learning Representations, 2017.
- [35] D.P. Kingma, J. Ba, Adam: A method for stochastic optimization, CoRR, Vol. abs/1412.6980, 2014.
- [36] D.P. Kingma, S. Mohamed, D.J. Rezende, M. Welling, Semi-supervised learning with deep generative models, in: Advances in Neural Information Processing Systems, 2014, pp. 3581–3589.

- [37] D.P. Kingma, T. Salimans, R. Jozefowicz, X. Chen, I. Sutskever, M. Welling, Improved variational inference with inverse autoregressive flow, in: *Advances in Neural Information Processing Systems*, 2016, pp. 4743–4751.
- [38] D.P. Kingma, M. Welling, Auto-encoding variational bayes., *CoRR*, Vol. abs/1312.6114, 2013.
- [39] A. Kucukelbir, D. Tran, R. Ranganath, A. Gelman, D.M. Blei, Automatic differentiation variational inference, *The Journal of Machine Learning Research*, Vol. 18, Iss. 1, 2017, pp. 430–474.
- [40] Y. LeCun, Y. Bengio, G. Hinton, Deep learning, *nature*, Vol. 521, Iss. 7553, 2015, p. 436.
- [41] Y. Lecun, L. Bottou, Y. Bengio, P. Haffner, Gradient-based learning applied to document recognition, Vol. 86, Dec. 1998, pp. 2278 – 2324.
- [42] Levine Jacob H., Simonds Erin F., Bendall Sean C., Davis Kara L., Amir El-ad D., Tadmor Michelle D., Litvin Oren, Fienberg Harris G., Jager Astraea, Zunder Eli R., Finck Rachel, Gedman Amanda L., Radtke Ina, Downing James R., Pe'er Dana, Nolan Garry P., Data-Driven Phenotypic Dissection of AML Reveals Progenitor-like Cells that Correlate with Prognosis, *Cell*, Vol. 162, Iss. 1, doi: 10.1016/j.cell.2015.05.047, feb, 2018, pp. 184–197.
- [43] L. Maaten, Learning a parametric embedding by preserving local structure, in: Dyk, D. van, Welling, M. (eds.), *Proceedings of the Twelfth International Conference on Artificial Intelligence and Statistics*, Hilton Clearwater Beach Resort, Clearwater Beach, Florida USA, 16–18 Apr, 2009, *Proceedings of Machine Learning Research* 5, PMLR, pp. 384–391.
- [44] L. van der Maaten, Accelerating t-SNE using Tree-Based Algorithms, *Journal of Machine Learning Research*, Vol. 15, 2014, pp. 3221–3245.
- [45] L. van der Maaten, G. Hinton, Visualizing data using t-SNE, *Journal of Machine Learning Research*, Vol. 9, 2008, pp. 2579–2605.
- [46] L. Van der Maaten, G. Hinton, Visualizing non-metric similarities in multiple maps, *Machine learning*, Vol. 87, Iss. 1, 2012, pp. 33–55.
- [47] L. van der Maaten, E. Postma, H. van den Herik, Dimensionality reduction: A comparative review.
- [48] A. Makhzani, J. Shlens, N. Jaitly, I. Goodfellow, Adversarial autoencoders, in: *International Conference on Learning Representations*, 2016.

- [49] S. Markidis, S.W. Der Chien, E. Laure, I.B. Peng, J.S. Vetter, Nvidia tensor core programmability, performance & precision, arXiv preprint arXiv:1803.04014, 2018.
- [50] L. McInnes, J. Healy, UMAP: Uniform Manifold Approximation and Projection for Dimension Reduction, ArXiv e-prints, Feb. 2018.
- [51] V. Mnih, K. Kavukcuoglu, D. Silver, A.A. Rusu, J. Veness, M.G. Bellemare, A. Graves, M. Riedmiller, A.K. Fidjeland, G. Ostrovski *et al.*, Human-level control through deep reinforcement learning, *Nature*, Vol. 518, Iss. 7540, 2015, p. 529.
- [52] H. Narayanan, S. Mitter, Sample complexity of testing the manifold hypothesis, in: *Advances in Neural Information Processing Systems*, 2010, pp. 1786–1794.
- [53] R.M. Neal, Annealed importance sampling, *Statistics and computing*, Vol. 11, Iss. 2, 2001, pp. 125–139.
- [54] J. Nickolls, I. Buck, M. Garland, K. Skadron, Scalable parallel programming with cuda, *Queue*, Vol. 6, Iss. 2, Mar. 2008, pp. 40–53.
- [55] S.J. Reddi, S. Kale, S. Kumar, On the convergence of adam and beyond, in: *International Conference on Learning Representations*, 2018.
- [56] D. Rezende, S. Mohamed, Variational inference with normalizing flows, in: Bach, F., Blei, D. (eds.), *Proceedings of the 32nd International Conference on Machine Learning*, Lille, France, 07–09 Jul, 2015, *Proceedings of Machine Learning Research* 37, PMLR, pp. 1530–1538.
- [57] D.J. Rezende, S. Mohamed, D. Wierstra, Stochastic backpropagation and approximate inference in deep generative models, in: Xing, E.P., Jebara, T. (eds.), *Proceedings of the 31st International Conference on Machine Learning*, Beijing, China, 22–24 Jun, 2014, *Proceedings of Machine Learning Research* 32, PMLR, pp. 1278–1286.
- [58] V. Rokhlin, Rapid solution of integral equations of classical potential theory, *Journal of computational physics*, Vol. 60, Iss. 2, 1985, pp. 187–207.
- [59] D.E. Rumelhart, G.E. Hinton, R.J. Williams, Learning internal representations by error propagation, *California Univ San Diego La Jolla Inst for Cognitive Science*, Techn. rep., 1985.
- [60] D.E. Rumelhart, G.E. Hinton, R.J. Williams, Learning representations by back-propagating errors, *nature*, Vol. 323, Iss. 6088, 1986, p. 533.
- [61] S. Santurkar, D. Tsipras, A. Ilyas, A. Madry, How Does Batch Normalization Help Optimization? (No, It Is Not About Internal Covariate Shift), ArXiv e-prints, May 2018.

- [62] S. Shalev-Shwartz, S. Ben-David, Understanding machine learning: From theory to algorithms, Cambridge university press, 2014.
- [63] D. Silver, A. Huang, C.J. Maddison, A. Guez, L. Sifre, G. Van Den Driessche, J. Schrittwieser, I. Antonoglou, V. Panneershelvam, M. Lanctot *et al.*, Mastering the game of go with deep neural networks and tree search, *nature*, Vol. 529, Iss. 7587, 2016, p. 484.
- [64] D. Silver, J. Schrittwieser, K. Simonyan, I. Antonoglou, A. Huang, A. Guez, T. Hubert, L. Baker, M. Lai, A. Bolton *et al.*, Mastering the game of go without human knowledge, *nature*, Vol. 550, Iss. 7676, 2017, p. 354.
- [65] S.L. Smith, P.J. Kindermans, Q.V. Le, Don't decay the learning rate, increase the batch size, in: International Conference on Learning Representations, 2018.
- [66] M.H. Spitzer, G.P. Nolan, Mass Cytometry: Single Cells, Many Features, *Cell*, Vol. 165, Iss. 4, 2016, pp. 780–791.
- [67] N. Srivastava, G. Hinton, A. Krizhevsky, I. Sutskever, R. Salakhutdinov, Dropout: a simple way to prevent neural networks from overfitting, *The Journal of Machine Learning Research*, Vol. 15, Iss. 1, 2014, pp. 1929–1958.
- [68] Stegle Oliver, Teichmann Sarah A., Marioni John C., Computational and analytical challenges in single-cell transcriptomics, *Nature Reviews Genetics*, Vol. 16, jan, 2015, p. 133.
- [69] J. Tang, J. Liu, M. Zhang, Q. Mei, Visualizing large-scale and high-dimensional data, in: Proceedings of the 25th International Conference on World Wide Web, International World Wide Web Conferences Steering Committee, 2016, pp. 287–297.
- [70] I. Tirosh, B. Izar, S.M. Prakadan, M.H. Wadsworth, D. Treacy, J.J. Trombetta, A. Rotem, C. Rodman, C. Lian, G. Murphy, M. Fallahi-Sichani, K. Dutton-Regester, J.R. Lin, O. Cohen, P. Shah, D. Lu, A.S. Genshaft, T.K. Hughes, C.G.K. Ziegler, S.W. Kazer, A. Gaillard, K.E. Kolb, A.C. Villani, C.M. Johannessen, A.Y. Andreev, E.M. Van Allen, M. Bertagnolli, P.K. Sorger, R.J. Sullivan, K.T. Flaherty, D.T. Frederick, J. Jané-Valbuena, C.H. Yoon, O. Rozenblatt-Rosen, A.K. Shalek, A. Regev, L.A. Garraway, Dissecting the multicellular ecosystem of metastatic melanoma by single-cell rna-seq, *Science*, Vol. 352, Iss. 6282, 2016, pp. 189–196.
- [71] J.M. Tomczak, M. Welling, Improving variational auto-encoders using householder flow, *CoRR*, Vol. abs/1611.09630, 2016.
- [72] L. Van Der Maaten, K. Weinberger, Stochastic triplet embedding, in: Machine Learning for Signal Processing (MLSP), 2012 IEEE International Workshop on, IEEE, 2012, pp. 1–6.



- [73] J. Venna, S. Kaski, Neighborhood preservation in nonlinear projection methods: An experimental study, in: Dorffner, G., Bischof, H., Hornik, K. (eds.), *Artificial Neural Networks — ICANN 2001*, Berlin, Heidelberg, 2001, Springer Berlin Heidelberg, pp. 485–491.
- [74] J. Venna, S. Kaski, Visualizing gene interaction graphs with local multidimensional scaling, in: *ESANN*, 2006.
- [75] R. Vershynin, *High-dimensional probability: An introduction with applications in data science*, Vol. 47, Cambridge University Press, 2018.
- [76] P. Vincent, H. Larochelle, I. Lajoie, Y. Bengio, P.A. Manzagol, Stacked denoising autoencoders: Learning useful representations in a deep network with a local denoising criterion, *Journal of machine learning research*, Vol. 11, Iss. Dec, 2010, pp. 3371–3408.
- [77] A.C. Wilson, R. Roelofs, M. Stern, N. Srebro, B. Recht, The marginal value of adaptive gradient methods in machine learning, in: *Advances in Neural Information Processing Systems*, 2017, pp. 4148–4158.
- [78] Y. Wu, Y. Burda, R. Salakhutdinov, R.B. Grosse, On the quantitative analysis of decoder-based generative models, *CoRR*, Vol. abs/1611.04273, 2016.
- [79] H. Xiao, K. Rasul, R. Vollgraf, Fashion-mnist: a novel image dataset for benchmarking machine learning algorithms, 2017.
- [80] Z. Yang, J. Peltonen, S. Kaski, Scalable optimization of neighbor embedding for visualization, in: *International Conference on Machine Learning*, 2013, pp. 127–135.
- [81] S. Zhao, J. Song, S. Ermon, Infovae: Information maximizing variational autoencoders, *arXiv preprint arXiv:1706.02262*, 2017.

## APPENDIX A: SMALL BATCH SIZE, LOW PERPLEXITY EMBEDDING

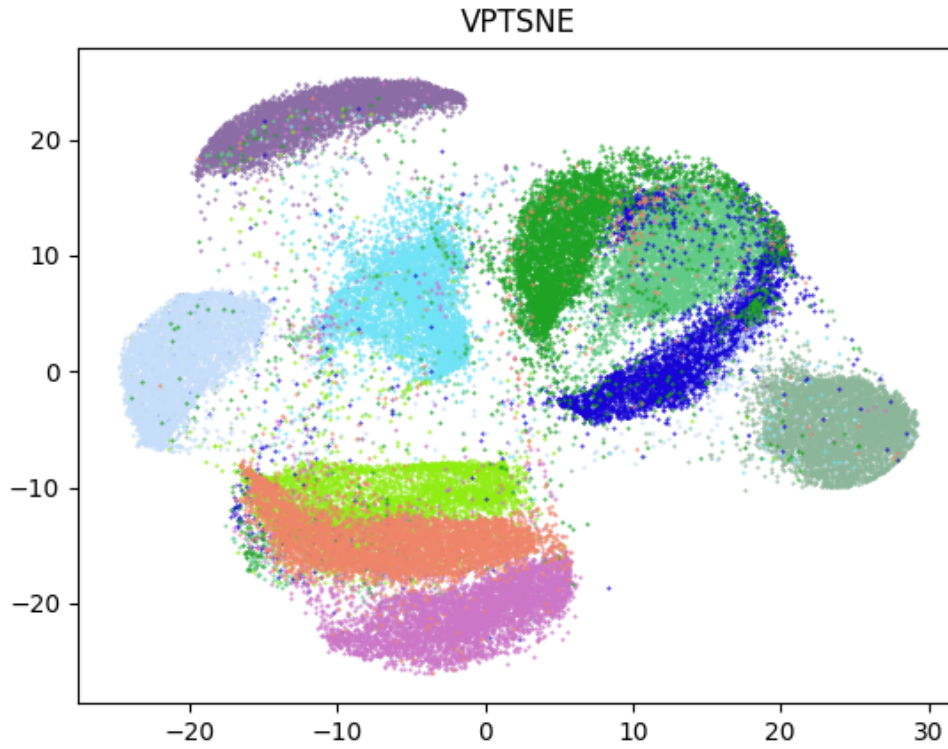


**Figure A.1.** Effect of the choice of perplexity w.r.t. batch size. MNIST VPTSNE embedding trained with batch size 200 and perplexity 10. Trustworthiness: 0.935, 1-NN: 0.812.

# APPENDIX B: UMAP EMBEDDING OF SCRNA-SEQ DATA

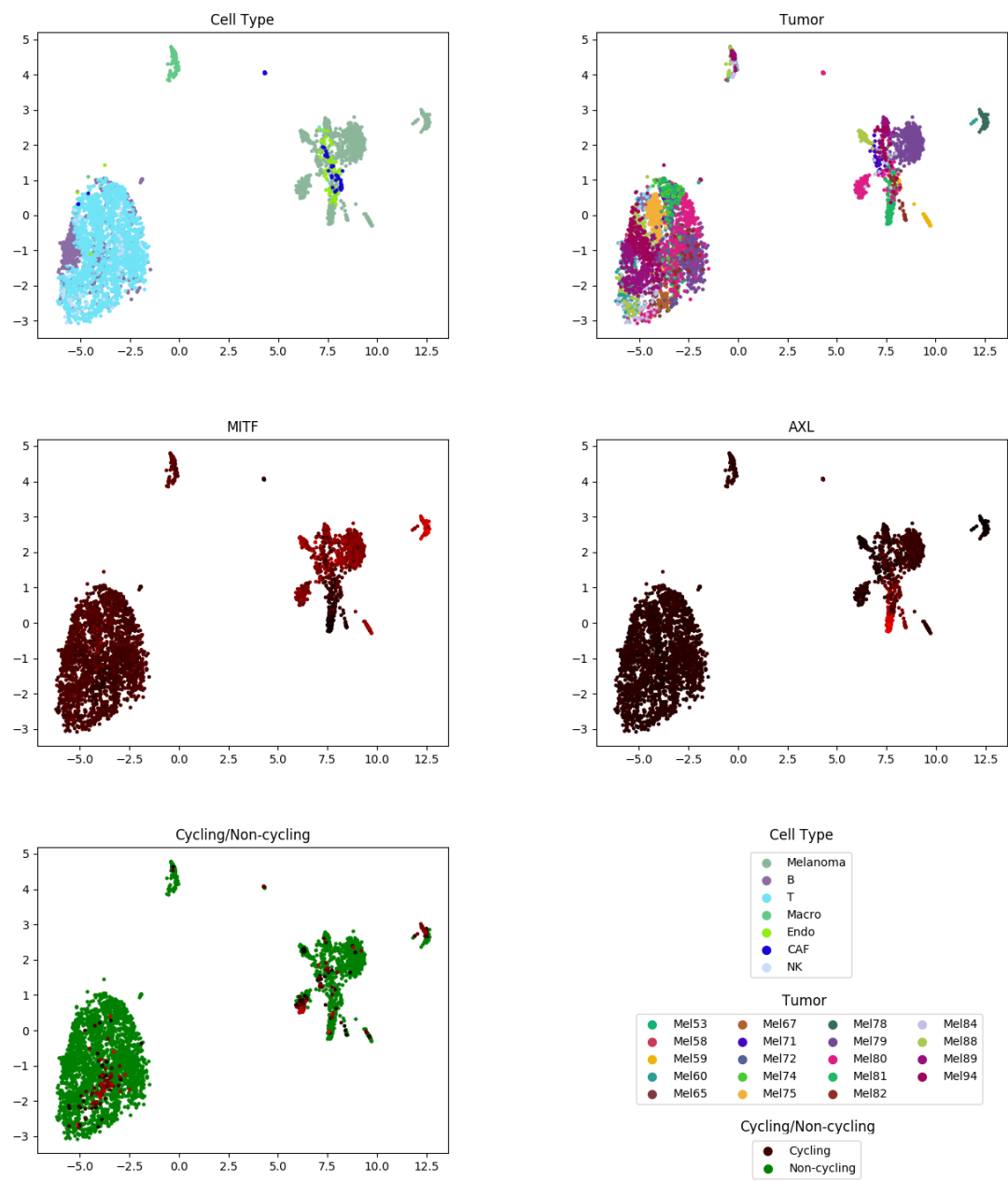


*Figure B.1. Visualization of analysis results on data from [70] using UMAP.*